The Pennsylvania State University

The Graduate School

College of Engineering

STABILITY ANALYSIS AND EXPERIMENTAL TESTING OF FLUIDIC PITCH LINKS IN HELICOPTERS WITH ARTICULATED ROTORS

A Dissertation in

Mechanical Engineering

by

Shawn M. Treacy

Submitted in Partial Fulfillment

of the Requirements

for the Degree of

Doctor of Philosophy

December, 2017

The dissertation of Shawn M. Treacy was reviewed and approved* by the following:

Christopher D. Rahn

Professor of Mechanical Engineering

Dissertation Co-Advisor, Co-Chair of Committee

Edward C. Smith

Professor of Aerospace Engineering

Dissertation Co-Advisor, Co-Chair of Committee

Joseph P. Cusumano

Professor of Engineering Science & Mechanics

Reuben H. Kraft

Professor of Mechanical Engineering

Karen Thole

Distinguished Professor of Mechanical Engineering

Department Head of Mechanical Engineering

*Signatures are on file in the Graduate School.

Abstract

Vibration levels in helicopters impact many aspects of flight including performance, comfort, and reliability. Three types of vibration control exist to dissipate these effects: passive control, semi-active control, and active control. Historically, rigid pitch links have been used on rotorcraft, however, researchers have been exploring alternatives to conventional rigid pitch links as a means to reduce vibrations. One viable passive vibration reduction device is the fluidic pitch link. Replacing rigid pitch links on rotorcraft with fluidic pitch links provides a method for vibratory control. At high frequencies, the pitch link impedance can be tuned to change the blade pitching response to higher harmonic loads. Although all have not been demonstrated simultaneously, fluidic pitch links have been shown to reduce rotor power and all six hub forces and moments. While reduced vibrations have been observed upon substitution of rigid pitch links for fluidic pitch links, the impact of fluidic pitch links on stability has not yet been examined. As such, this investigation explores the aeroelastic stability of a helicopter with fluidic pitch links.

Each rotor is articulated and is modeled by rigid pitch and rigid flap degrees of freedom. Quasi-steady aerodynamics are used for the lift and moment terms in the aeroelastic model. The control system stiffness is modeled as an axial spring. The fluidic pitch links have two degrees of freedom: axial displacement of the piston, which is directly related to pitch, and volume of fluid entering the inertia track. A positive impact on aeroelastic stability from several fluidic pitch link designs is demonstrated for hover. The positive stability margins found for the fluidic pitch links in hover are marginally affected by the periodic terms that appear in forward flight. The fluidic pitch links are shown to help stabilize the pitch mode and enable use of substantially larger aft center of gravity offsets in rotor design.

To test the fluidic pitch link for model verification purposes, the model for a double pumper fluidic pitch link was derived. This is a more viable and popular choice than the single pumper design used previously due to greater safety and reduced risk of cavitation. A prototype fluidic pitch link was designed, built, and

tested at LORD Corporation. Displacement, load, and pressure were recorded during testing. Frequency and time response results were compared between simulation and experiment to validate the model. Three different fluid circuits were used, and the model accurately predicted performance for each of them with the exception of inaccuracy at low frequency due, in part, to the frequency dependence of the elastomer. An additional fourth circuit was tested that included a needle valve. The model did not accurately predict results across the entire range of valve positions, but the model was able to accurately match the dynamic stiffness amplitude using empirical parameters from a parameter study.

Table of Contents

List of Figures

List of Tables

List of Symbols

A	Piston cross-sectional area
A_{FT}	Fluid track cross-sectional area
c	Blade chord
$[C]$	Generalized damping matrix
C	Theodorsen's lift deficiency function
C'	Loewy's lift deficiency function
C_a	Accumulator capacitance
C_b	Bottom chamber capacitance
c_d	Elastomer damping
c_f	Equivalent fluid damping
C_p	Upper chamber capacitance
C_t	Top chamber capacitance
C_ζ	Lag damping
D	Fluid track inner diameter
F	Axial force on pitch link
I	Fluid inertance
I_b	Blade flap inertia
I_f	Blade feathering inertia
I_u	Uncorrected fluid inertance
I_ζ	Generalized mass of the fundamental lag mode
$[K]$	Generalized stiffness matrix
K_b	Stiffness due to the bottom fluid chamber capacitance
K_{pl}	Pitch link axial stiffness
K_L	Pitch-lag coupling
K_{LC}	Stiffness due to the capacitance in the accumulator
K_p	Pitch-flap coupling

K_t	Stiffness due to the top fluid chamber capacitance
K_{UC}	Stiffness due to the capacitance in the upper chamber
K_β	Flap spring torsional stiffness
K_θ	Pitch spring torsional stiffness
K^*	Dynamic or complex stiffness
K'	Real part of the dynamic stiffness
K''	Imaginary part of the dynamic stiffness
k_d	Elastomer stiffness
k_{ss}	Fluidic pitch link static stiffness
L	Fluid track length, section aerodynamic lift force
l_{ph}	Length of the pitch horn
$[M]$	Generalized mass matrix
M_a	Section aerodynamic pitch moment
m_b	Blade mass per unit length
m_c	Mass of the outer can
m_f	Equivalent fluid mass
m_p	Mass of the piston
M_β	Aerodynamic flap moment
M_θ	Aerodynamic pitch moment
$M_{\theta_{FPL}}$	Pitch moment due to the fluidic pitch link
N_b	Helicopter number of blades
p	Pressure in the upper chamber
p_a	Pressure in the accumulator
p_b	Pressure in the bottom chamber
p_t	Pressure in the top chamber
R	Blade radius
R_f	Fluid resistance
R_{fu}	Uncorrected fluid resistance
r	Blade radial coordinate
r_0	Fluid track inner radius
T	Period of the system
u_P	Air velocity perpendicular to the disk plane
u_R	Air velocity of radial blade section
u_T	Air velocity tangent to the disk plane
V	Volume of fluid that enters the fluid track
x	Piston displacement, non-dimensional blade radial coordinate
x_I	Chordwise offset of blade center of gravity behind pitch axis
z	Displacement of fluid into the inertia track
α	Non-dimensional correction factor for calculating fluid resistance and inertance
β	Blade flap angle

β_0	Blade precone angle
γ	Blade Lock number
Λ	Characteristic exponent
λ	Eigenvalue or characteristic multiplier, rotor inflow ratio
μ	Dynamic viscosity
ν	Kinematic viscosity
Ω	Rotor rotational speed
ω	Frequency of oscillation
ω_n	Natural frequency
ω_β	Flap natural frequency
ω_θ	Pitch natural frequency
ω_ζ	Lag natural frequency
ρ	Fluid density
σ	Stability margin
σ_β	Flap stability margin
σ_θ	Pitch Stability margin
θ	Blade pitch angle
θ_0	Collective pitch angle
ζ_{FPL}	Fluidic pitch link damping ratio
ζ_β	Flap damping ratio
ζ_θ	Pitch damping ratio
$(\ )^*$	Non-dimensionalized by I_b
$\overline{(\ )}$	Non-dimensional parameter
$\overset{*}{(\ )}$	Non-dimensional derivative

Acknowledgments

Many people have encouraged and helped along the way throughout my graduate studies. I would first like to thank my advisors, Dr. Christopher Rahn and Dr. Edward Smith, for their help and guidance. My fellow lab mates, in particular Mayank Garg and Matt Krott, deserve much thanks for their help, insight, and support, as well.

I would also like to thank Dr. Mark Jolly and Dr. Conor Marr of LORD Corporation for their technical guidance and LORD Corporation for the financial support along the way. Additional invaluable technical support was also provided by Fred Claflin, Chad Rudinski, Aric Szklenski, and Ben Ryan-Lorei.

Finally, I would like to thank my friends and family for supporting me throughout graduate school and always being there for me when I needed them most.

Chapter 1

Introduction and Background

Vibration levels in helicopters impact many aspects of flight including performance, comfort, and reliability. Oscillatory motion of the rotor causes component fatigue, which can lead to a decrease in aircraft availability and an increase in maintenance costs. Vibration levels also affect crew and passenger comfort. Typical passenger acceleration levels range from 0.10–0.15g range while ideal values are less than 0.05g.

Vibratory loads in the fuselage are mainly due to the main rotor unsteady aerodynamic environment interacting with flexible blades. The rotor, however, acts to filter the forces between the rotor and fuselage as can be shown using a Fourier Coordinate Transformation or Multi-Blade Coordinate Transformation from the rotating to the fixed frame [2]. Loads measured in the rotating frame are observed in the fixed frame of the fuselage at integer multiples of $N_b\Omega$ where N_b is the number of blades and Ω is the rotor rotation frequency. The most dominant frequency felt in the cabin is N_b/rev. The coordinate transformation shows that rotating frame $(N_b \pm 1)/rev$ in-plane blade root shears in the radial and lagwise directions result in N_b/rev in-plane hub forces in the fixed frame. Similarly, N_b/rev torsional and flapwise root moments in the rotating frame result in N_b/rev pitch and roll

moments in the fixed frame.

One method for vibration reduction in helicopters involves ensuring that the airframe and rotor resonant frequencies have adequate separation. However, ensuring this frequency separation does not adequately reduce vibration levels [3]. As such, additional techniques for controlling vibration in a helicopter have been developed and are expanded upon in Section 1.1. Additionally, upon application of vibration treatments, it is critical to ensure that the helicopter remains stable, especially if the treatments interact with the rotor. Aspects of the aeroelastic stability of helicopters are discussed in Section 1.2.

1.1 Vibration Control

There are three primary types of vibration control: passive control, semi-active control, and active control. Passive control techniques are typically designed to modify the stiffness or damping of a structure without requiring an external power source. With semi-active control, the characteristics of a device can be changed continually, chosen within a range of pre-established values, or changed in response to environmental conditions such as a machine being turned on or off. An active control system uses a large external power source, sensors, and control actuators to apply force to either add or dissipate energy in a structure [4].

1.1.1 Passive Control

There are three common passive types of control devices: damper, dynamic vibration absorber, and vibration isolator. A mechanical damper typically uses friction to dissipate vibrational energy in a system as heat [5]. Some common passive damping

devices include fluid dampers, eddy currents, elastomers or hysteretic elements [6], piezoelectric shunt circuits, and viscoelastic layers [7].

A dynamic vibration absorber is an oscillator such as a mass and spring that is tuned to a specific system vibration frequency in order to receive a significant portion of the vibrational energy from the primary system at that frequency. In turn, the resulting vibration from the absorber applies an oscillatory force that opposes the system vibration to cancel out its effect [8]. Within a helicopter, a typical Frahm vibration absorber with a mass and spring is often used in the fuselage such as the one in the Bell Model 427 [9] while pendulum style vibration absorbers such as the bifilar first found on the Sikorsky S-61 can be attached to the rotor [10]. Damping can also be included with an absorber to create a damped absorber or tuned mass damper [11, 12]. The original Frahm device does not have any inherent damping, so if the system deviates from the tuned frequency towards the system resonant frequencies, it will respond with large amplitude vibrations. Addition of damping to the system makes it possible to curb the performance deterioration that occurs when the excitation frequency changes [13]. By placing pendulum absorbers in a centrifugal field, it easily allows for the tuning of the absorber to a frequency that is a multiple of the rotation speed. However, a practical problem exists with the simple pendulum design in which the required short pendulum length cannot physically coexist with the size of the required mass to be effective at higher frequency. Chilton's invention, the bifilar absorber, solved this problem. It was originally designed to reduce torsional vibration in reciprocating aircraft engines and was later extended to helicopter applications. The bifilar pendulum is typically a U-shaped weight that fits loosely around an arm that is projecting from the center of rotation [14]. A lightweight vibration absorber using coupled

fluidic flexible matrix composite (F^2MC) tubes has also been developed to reduce vibrations in the helicopter tailboom [15, 16].

Vibration isolators use a load-supporting component such as a spring and an energy dissipating component such as a dashpot placed between an excitation source and a system to reduce the transmitted load [17]. One of the first isolators used in helicopters, the Kaman dynamic antiresonant vibration isolator (DAVI), resolves the difficulty that conventional isolators had in dealing with low frequency isolation. The main challenge encountered with convential isolators involves the need for large static deflections to attenuate low frequency vibrations. However, the isolator would then bottom out during shock loads causing large loads to be transmitted to the isolated system. The DAVI solved this problem using rotary inertial coupling between the input and output by applying a mass to a bar that is perpendicular to the direction of vibration. A spring then connects the mass to the base where the excitation takes place. This configuration enables the DAVI to provide a high degree of isolation at low frequency while maintaining small deflections. This device can be attached to a passenger seat to isolate the passenger from the fuselage vibration [18]. More compact devices such as the Bell liquid inertia vibration eliminator (LIVE®) [19] and LORD Fluidlastic® isolators [20] have taken advantage of the mechanical properties espoused by the DAVI while using a smaller footprint. This was accomplished by using an elastomer attached to a piston and forcing a fluid through an inertia track [9]. This technology is also able to handle vibration cases in which very high static stiffness is needed with a low effective dynamic stiffness at the N/rev isolation frequency, as required by the pylon isolation system in the Augusta A109E that used LORD Fluidlastic® isolators [21].

1.1.2 Semi-Active Control

Anusonti-Inthra and Gandhi used a simulation to show that semi-active hydraulic lag and flap dampers can be used to reduce higher harmonic vibratory hub loads through cyclic control of variable orifice dampers [22]. This work was adopted by Titurus and expanded upon in [23–26]. Hiemenz uses a magnetorheological energy absorber that may be used in the suspension of passenger seats to automatically accomodate occupants of varying weight [27]. Variable stiffness F^2MC tubes employ a valve that controls a variable orifice and are designed for semi-active vibration control [28, 29]. Other smart structures such as those devices that use a semi-active control law to switch the piezoelectric shunt circuit of a piezoelectric actuator between open-circuit and short- or resistive-circuit in order to vary stiffness can be used for vibration control [30].

1.1.3 Active Control

Helicopter active control technologies can be divided into two categories: those that are airframe-based and those that are rotor-based. Airframe based control approaches do not reduce vibration at the source. Rather, the vibration caused by an external force is opposed and canceled by applying an actuator response to the airframe. Rotor based control technologies treat vibration due to the unsteady loads being generated by the main rotor at the source [31].

One such airframe-based control technology is the airframe-mounted self-tuning vibration absorber designed by Sikorsky. The technology uses two bifilar pendulum mounted masses that act under controllable spring forces in order to automatically control the natural frequency [32]. Another method is the active control of structural response (ACSR) system developed by Westland Helicopter. This system

uses electro-hydraulic actuators that are mounted across the airframe and main transmission interface. A digital control computer receives data from accelerometers that are mounted at key points around the fuselage and a control algorithm is applied in order to minimize vibration [33–35].

Among rotor-based active control technologies, higher harmonic control (HHC) has received the most attention. HHC involves actuating a conventional swashplate in the non-rotating frame at N_b/rev, which modifies the vibratory loads at the blade using pitch control, to reduce vibratory levels in the fuselage and at the hub [36–38]. This technology has been demonstrated in the wind tunnel [39] and with flight tests [40, 41]. However, it has yet to be implemented on a production helicopter due to various issues including degrading rotor performance, significant power requirements, high cost, and limitations on effectiveness for hingeless and bearingless rotors [42].

Individual blade control (IBC), an alternative to HHC, involves using an actuator between the swashplate and blade to individually control each blade in the rotating frame with a feedback loop. This enables the IBC technology to control a wider range of frequencies than HHC [43–45]. A full-scale wind tunnel test [46, 47] and flight test [48] have demonstrated the utility of the technology by replacing pitch links with controllable actuators. However, numerous challenges still exist including the likelihood that a production helicopter would require replacing a conventional swashplate with an electronic one, a drastic step that could only be justified in the case of unequivocal advantages [42].

Other active approaches to rotor control include using trailing edge flaps (TEFs) along each individual blade or a hub mounted vibration supressor (HMVS). Trailing edge flaps demonstrate similar vibration reduction as conventional IBCs but with a

reduction in power required [49]. Control effort can be reduced even further by a hybrid optimization of the blade structure and the flap controller [50]. TEFs can also reduce the power required in the rotor. This was demonstrated using multiple spanwise TEFs [51]. The prototype dual-frequency HMVS was demonstrated at a LORD Corp. test facility on a CH-3 fuselage that led to ground and flight testing on a Sikorsky UH-60A Blackhawk helicopter. The HMVS was used to nullify fuselage N/rev vibrations due to in-plane vibratory hub loads. The testing revealed that the system successfully matched or exceeded performance of the existing passive systems at a significant weight savings [52].

1.2 Aeroelastic Stability

Aeroelastic stability refers to the stability of a helicopter due to the blade response whereas aeromechanical stability refers to the coupled rotor/fuselage problem. This section expounds upon the stability of individual blades and focuses on the stability problems that exist, the degrees of freedom that are required, and the assumptions that can be made.

1.2.1 Pitch-Flap Stability

Miller and Ellis developed the groundbreaking work that covers much of the pitch-flap flutter problem in hover [53]. Their focus was on an articulated (hinged) rotor with pitch and flap degrees of freedom. The problem is similar to the classical bending/torsion flutter analysis that was known to fixed wing researchers but is augmented by inertial and aerodynamic terms due to rotation of the blade. Their findings elucidated the importance of either increasing the torsion natural frequency

or moving the blade chordwise center-of-gravity forward in the blade in order to maintain a stable system. Most blade designs today place the chordwise center of gravity at or forward of the quarter-chord in order to avoid this instability. The study also showed that steady in-plane bending has a minor effect on stability of an articulated rotor while steady elastic in-plane deflections can have a major impact on the stability of articulated rotors with a non-uniform spanwise mass distribution. Additionally, Miller and Ellis demonstrated the significant impact of pitch-flap coupling on stability and that unsteady aerodynamics have a minor effect on the stability boundary.

1.2.2 Pitch-Lag Stability

Chou performed a comprehensive analysis of the pitch-lag stability of an articulated rotor with inelastic blades [54]. He found that the instability was caused by the pitch-lag coupling introduced by skewing the lag hinge outboard of the flap hinge and developed a stability criterion for the design of stable blades,

$$\frac{(C_\zeta + 2K_L\beta_0^2\Omega I_\zeta)}{\left(1 - \frac{\beta_0}{\theta_0}K_p\right)\theta_0} > 0. \tag{1.1}$$

C_ζ is the lag damping. K_L is the pitch-flap coupling. β_0 is the coning angle. Ω is the rotation frequency. I_ζ is the generalized mass of the fundamental lag mode. θ_0 is the collective pitch. K_p is the pitch-flap coupling.

1.2.3 Flap-Lag Stability

The flap-lag instability is most important for tilt, hingeless, and bearingless rotors. It is also the most complicated due to the need to capture the effects of the

nonlinear coupling between flap and lag degrees of freedom caused by aerodynamic and coriolis effects [55].

Numerous unsteady aerodynamic theories were developed out of the need for a better representation of the aerodynamics to accommodate the complex, unsteady environment of the blade. Loewy [56] was the first to create a rotary wing aeroelastic unsteady aerodynamic theory for hover, a generalization to rotary wing aeroelasticity of a previous work completed by Theodorsen [57]. Greenberg also developed another theory that modified Theodorsen's work to apply to rotary wing problems [58]. Several issues exist with these early studies stemming from the assumption of simple harmonic motion and the frequency domain results. The assumption of simple harmonic motion was only valid at the stability boundary and provided no information pertaining to the system damping before or after flutter. Additionally, since these theories were created for the frequency domain, they are not suitable for forward flight analyses. Ultimately, these studies were extended to the time domain in [59] for Theodorsen's theory, [60] for Loewy's theory, and [61] for Greenberg's theory. Accurate modeling of unsteady aerodynamics continues to be a challenge due to: complicated flowfield, time-varying geometry of wake is complex, problems of transonic flow at large advance ratios, shock waves occuring on the advancing tip, reverse flow, and low-speed unsteady stall on the retreating blade. Modern swept and curved-tip blade geometries further complicate these problems [55].

Young was the first to develop equations of motion for the flap-lag problem in hover and forward flight [62]. However, this work lacked consistency in including terms of the same order, so it provides some correct and some incorrect statements about the stability criteria. A similar work by Hohenemser [63] made congruent

errors with qualitative results. These works failed to capture the critical importance of elastic and structural coupling between the flap and lag degrees of freedom that were demonstrated and available in [64].

Ormiston and Hodges [65] provided the best treatment in hover. They used a simple centrally hinged, spring-restrained model of a hingeless blade with no hinge offset and a torsionally rigid blade. They demonstrated that the instability could be eliminated by elastically coupling blade bending in and out of the plane of rotation and that small amounts of structural damping helped to eliminate the instability [66]. These results were verified in an experiment [67] and the study was ultimately extended to forward flight [68].

1.2.4 Flap-Lag-Torsion Stability

The flap-lag-torsion model of a hingeless blade produces the most realistic, yet most complicated, equations. This model builds on the flap-lag model to include the torsion degree of freedom. Hingeless blades can be split into two types: soft-in-plane rotors in which the lag frequency is lower than the rotational frequency (typically near $0.7/rev$) and stiff-in-plane rotors in which the lag frequency is greater than the rotation frequency ($\frac{\omega_\zeta}{\Omega} > 1$). Studies have demonstrated that soft-in-plane hingeless rotors are usually stable. The only instability that occurs is due to the presence of precone and is a flap-lag type of instability that is referred to as precone induced flap-lag instability [69–71]. The equations of motion in forward flight can be found in [72]. These equations demonstrate the effect of forward flight on the stability of hingeless rotors. Forward flight was found to be stabilizing for soft-in-plane hingeless rotors and severely destabilizing for stiff-in-plane hingeless rotors [73].

1.3 Comprehensive Codes

The complexity of rotary wing aeroelasticity problems motivated the development of computer codes capable of solving both isolated blade and coupled rotor-fuselage problems called comprehensive analysis codes [55]. These codes also include calculations for performance and flight mechanics. The first code was developed in the 1970s by Lockheed and is called REXOR [74]. The first widely successful code developed is CAMRAD by Johnson [75, 76]. This code was improved upon and succeeded by CAMRAD/JA [77, 78], which was further improved and has ultimately become CAMRAD II [79]. An additional sophisticated code, Second Generation Computational Helicopter Analysis Systems (2GCHAS), was developed with funding by the U.S. Army Aeroflightdynamics Directorate and is the successor to REXOR [80]. This code has since been modified and refined further to incorporate a more accurate nonlinear beam element over the one used in 2GCHAS. This improved code is known as the Rotorcraft Comprehensive Analysis Code (RCAS) [81]. A well-known multi-flexible-body code, DYMORE, has extensive capability in modeling of system hardware [82]. A more extensive survey of comprehensive analyses can be found in a review by Johnson [83].

1.4 Present Research

Fluidic pitch links, passive vibration reduction devices, have been and continue to be investigated for their potential to replace current rigid pitch links. A pitch link is a rigid rod with spherical end bearings that connects the swashplate to the pitch horn, which is in turn connected to the blade root. An example of a conventional pitch link for a light duty helicopter with a hingeless rotor and axial bearings for

pitch motion is pictured in Figure 1.1 to illustrate these connections. When the pilot moves the collective pitch lever, a static or 0/rev event, the swashplate moves vertically thus pitching all four blades equally and changing the thrust magnitude. When the pilot moves the cyclic pitch stick, a 1/rev event, the swashplate angles thus changing the thrust direction. Additionally, there are higher harmonic aerodynamic blade excitations at 2/rev and higher frequencies that load the pitch link. These excitations can lead to high pitch link loads, which can limit maximum forward speed and may pose fatigue and vibration challenges [84]. Fluidic pitch links have shown promise as a means to reduce vibration and improve stability beyond the levels of a traditional rigid pitch link.

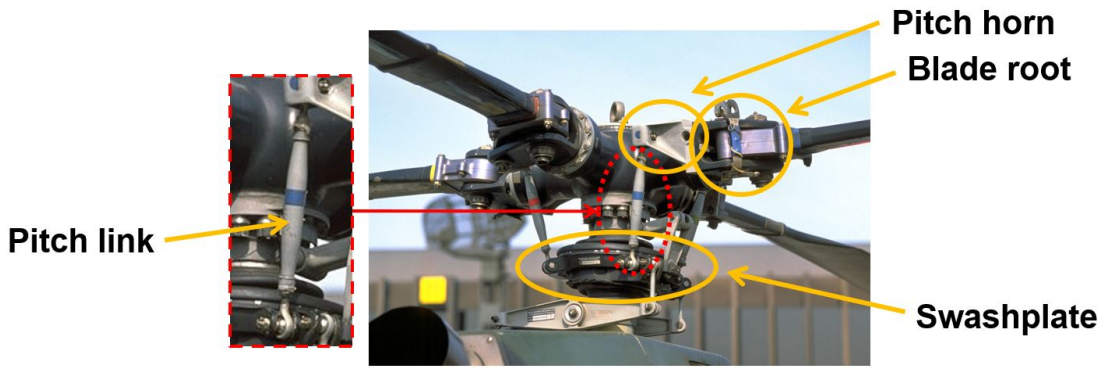

Figure 1.1: MBB Bo105 main rotor head and swashplate assembly. Adapted from ©1988 Burkhard Domke [1] and used with permission.

Scarborough et al. [85] examined impedance tailoring fluidic pitch links for reduction of hub loads in high speed flight conditions. A rotor aeroelastic simulation demonstrated the ability to influence all six of the hub forces and moments as well as a modest decrease in rotor power. Zhang et al. [86] expanded upon the work completed by Scarborough et al. by adding a free wake model in order to explore low forward speed. The results continue to exhibit the potential for vibratory control. While these studies explore vibration, the effect of this vibration treatment

on aeroelastic stability has not been examined.

Acccordingly, the objective of this study is to explore the impact of fluidic pitch links on the aeroelastic stability in hover and forward flight of an articulated rotor on a medium-duty helicopter similar to the UH-60. In this model, the blade is treated as rigid with two degrees of freedom in pitch and flap. The fluidic pitch links are modeled with two degrees of freedom: axial displacement of the piston, which is directly proportional to rigid pitch, and volume of fluid entering the inertia track. One additional degree of freedom reflects the flexibility in the control system and yields a four degree of freedom system. In addition to simulating the stability of a rotor with fluidic pitch links, testing was completed to obtain the veracity of the fluidic pitch link model.

Chapter 2

Pitch-Flap Stability of an Articulated Rotor with Fluidic Pitch Links

2.1 Introduction

Researchers have been exploring alternatives to conventional rigid pitch links in order to reduce rotorcraft hub and pitch link vibration, increase pilot comfort, and extend component life. Milgram et al. [87] analyzed replacing conventional pitch links with a spring and damper element. The spring and damper element showed moderate improvements in hub loads. Han et al. [88], inspired by the work of McGuire in [20] that introduced Fluidlastic® dampers and isolators for vibration control in helicopters, explored using a Fluidlastic® isolator to reduce pitch link loads. The authors were able to show a significant reduction in higher harmonic pitch link loads ultimately demonstrating more than a 98% reduction in 4/rev pitch link loads in high forward speed. Scarborough et al. [85] examined impedance

tailoring fluidic pitch links (FPLs) for reduction of hub loads in high speed flight conditions. A rotor aeroelastic simulation showed the ability to influence all six of the hub forces and moments as well as a modest decrease in rotor power. Zhang et al. [86] expanded upon the work completed by Scarborough et al. by adding a free wake model in order to explore low forward speed. The results continue to show the potential for vibratory control. While all of these studies focus on vibration, they do not examine the effect of the vibration treatments on *aeroelastic stability*.

As pointed out by Chopra [89], a landmark work by Miller and Ellis [53] in the 1950s initially demonstrated how to find the stability boundaries for an articulated rotor in hover while Ham [90] performed an encompassing review of this topic that includes hover and forward flight in the early 1970s. Both works demonstrated the need for the center of gravity of the blade to be placed at or forward of the aerodynamic center to avoid a pitch-flap flutter instability. Johnson discusses the perturbation equations of motion for the rigid pitch and rigid flap degrees of freedom in hover and forward flight [91] as well as the classical pitch-flap stability in hover [92]. The state of the art involves use of comprehensive analyses such as RCAS, CAMRAD II, and HOST as were used in [93] to analyze the aeroelastic stability of two hingeless rotors.

The objective of this chapter is to explore the impact of fluidic pitch links on the aeroelastic stability in hover and forward flight of an articulated rotor on a medium-duty helicopter similar to the UH-60. In this model, the blade is treated as rigid with two degrees of freedom in pitch and flap. The fluidic pitch links are modeled with two degrees of freedom: axial displacement of the piston, which is proportional to rigid pitch, and volume of fluid entering the inertia track. There is one additional degree of freedom due to flexibility in the control system to obtain a

four degree of freedom system.

2.2 Aeroelastic and Fluidic Pitch Link Modeling

The aeroelastic equations of motion for the system are derived in two parts. The first part in [94] covers the dynamics while unsteady aerodynamics from the analysis presented in [95] are used to calculate the lift and aerodynamic moment. The unperturbed equations are listed in Eqs. (A.1–A.7). The degrees of freedom of the equations of motion are then perturbed to obtain the final form of the equations as performed in [91]. The articulated rotor is modeled with two degrees of freedom in rigid pitch and rigid flap. Lag motion is neglected for the articulated rotor, but it would be necessary to include when exploring the stability of a hingeless rotor [92]. The pitch bearing is assumed to be outboard of the flap hinge. A trailing pitch link is used. A schematic of a blade segment with attached FPL is illustrated in Figure **??**. I_f is the blade feathering inertia, which will be non-dimensionalized by the blade flapping inertia, I_b. Some assumptions will be made to simplify the model: the fuselage is infinitely stiff and thus can be assumed rigid; the pitch bearing stiffness is low compared to the pitch link and control system stiffnesses and can thus be neglected; the blade is rigid and uniform; the lift is much larger than the drag; blade flapping, inflow angle, blade pitch, and blade angle of attack are small; angle of attack is varied linearly with lift; radial flow effects are neglected; insignificant terms in the aerodynamic loads such as the virtual mass terms are dropped; and the aerodynamic center is assumed to be at the quarter chord.

The FPL model was developed in [85] and is illustrated in Figure 2.2 with an attached spring representing the control system stiffness. The elastomer has stiffness, k_d, and damping, c_d. The piston has cross-sectional area, A, and mass,

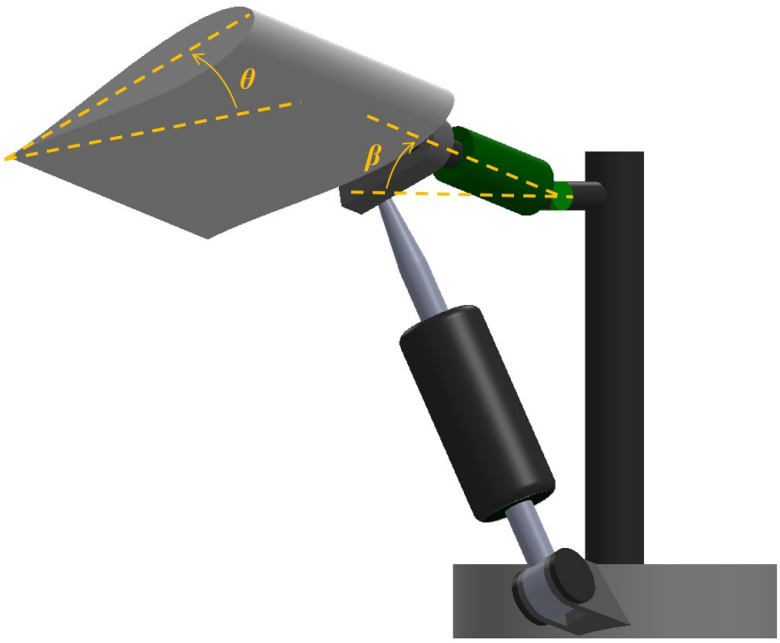

Figure 2.1: Rotor blade segment with attached fluidic pitch link demonstrating pitch and flap degrees of freedom.

m_p. The upper chamber has capacitance, C_p, and pressure, p. The inertia track has volume, V; cross-sectional area, A_{FT}; inertance, I; and fluid resistance, R_f. The lower chamber has capacitance, C_a, and pressure, p_a. By assuming that the area of the fluid track, A_{FT}, is much less than the piston cross-sectional area, a mechanical analogy has been developed and is illustrated in Figure 2.3. The displacement of the fluid entering the inertia track is z. An equivalent fluid mass, m_f, and equivalent fluid damping, c_f, are used. The capacitance in the upper chamber and accumulator are represented by springs K_{UC} and K_{LC}, respectively.

The fluid flow equations for the FPL are:

$$p - p_a = I\ddot{V} + R_f\dot{V}, \tag{2.1}$$

$$p_a = \frac{1}{C_a}V, \tag{2.2}$$

$$p = \frac{1}{C_p}\left[A\left(x-y\right)-V\right]. \tag{2.3}$$

The FPL equations of motion are:

$$I\ddot{V} + R_f\dot{V} + \left(\frac{1}{C_a}+\frac{1}{C_p}\right)V + \frac{A}{C_p}\left(y-x\right) = 0, \tag{2.4}$$

$$m_p\ddot{x} + c_d\left(\dot{x}-\dot{y}\right) + \left(k_d + \frac{A^2}{C_p}\right)\left(x-y\right) - \frac{A}{C_p}V = F, \tag{2.5}$$

$$\begin{aligned} m_c\ddot{y} + c_d\left(\dot{y}-\dot{x}\right) + \left(k_d + \frac{A^2}{C_p} + K_{cs}\right)y \\ - \left(k_d + \frac{A^2}{C_p}\right)x + \frac{A}{C_p}V = 0. \end{aligned} \tag{2.6}$$

Eq. (2.4) is the fluid flow equation. It results from the combination of Eqs. (2.1–2.3). Eq. (2.3) is the mechanical-fluidic coupling term. Eq. (2.5) is the internal force equation on the piston. Eq. (2.6) is the force summation on the outside can of the FPL. The first degree of freedom is the vertical motion of the piston. The top of the pitch link is attached to the pitch horn, which is connected to the blade root. It is assumed that these connections are rigid and thus the displacement of the piston is directly proportional to the blade-root pitch,

$$x = l_{ph}\theta. \tag{2.7}$$

Eq. (2.4) is then multiplied by the pitch horn length, l_{ph} to obtain the corresponding pitch moment due to the FPL,

$$M_{\theta_{FPL}} = l_{ph}F, \tag{2.8}$$

and will add into the rotor equation of motion for pitch. The second degree of

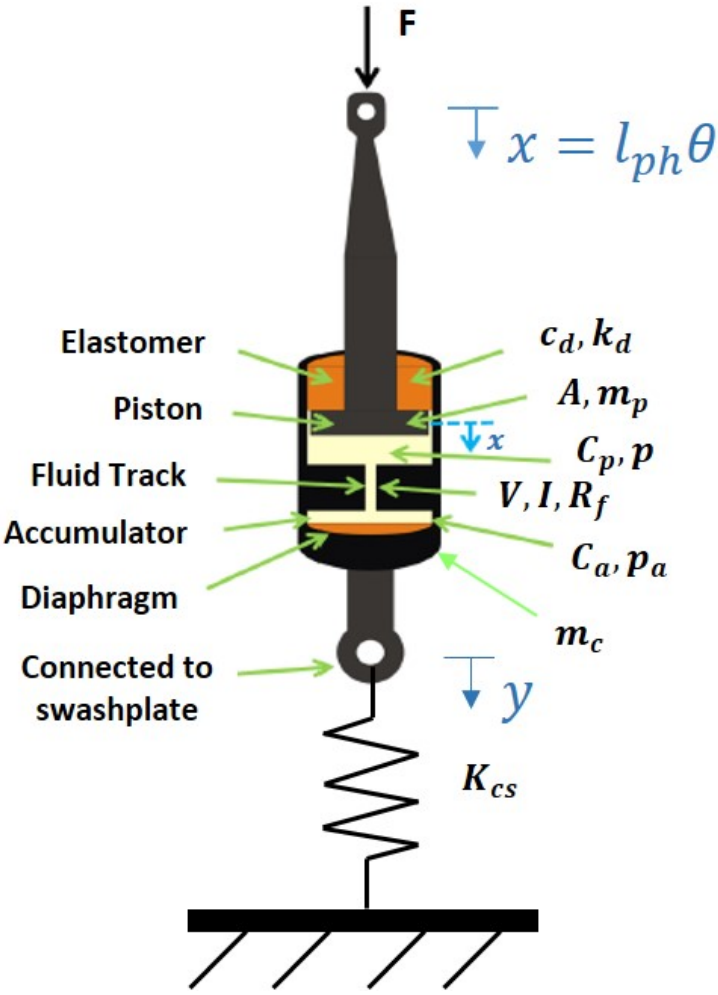

Figure 2.2: Fluidic pitch link model.

freedom is the volume displaced into the fluid track. The third degree of freedom is due to the motion of the bottom of the FPL, which is attached to the swashplate. The full model is four degrees of freedom in flap, pitch, displacement of the bottom of the FPL, and volume displaced into the inertia track. The non-dimensionalized

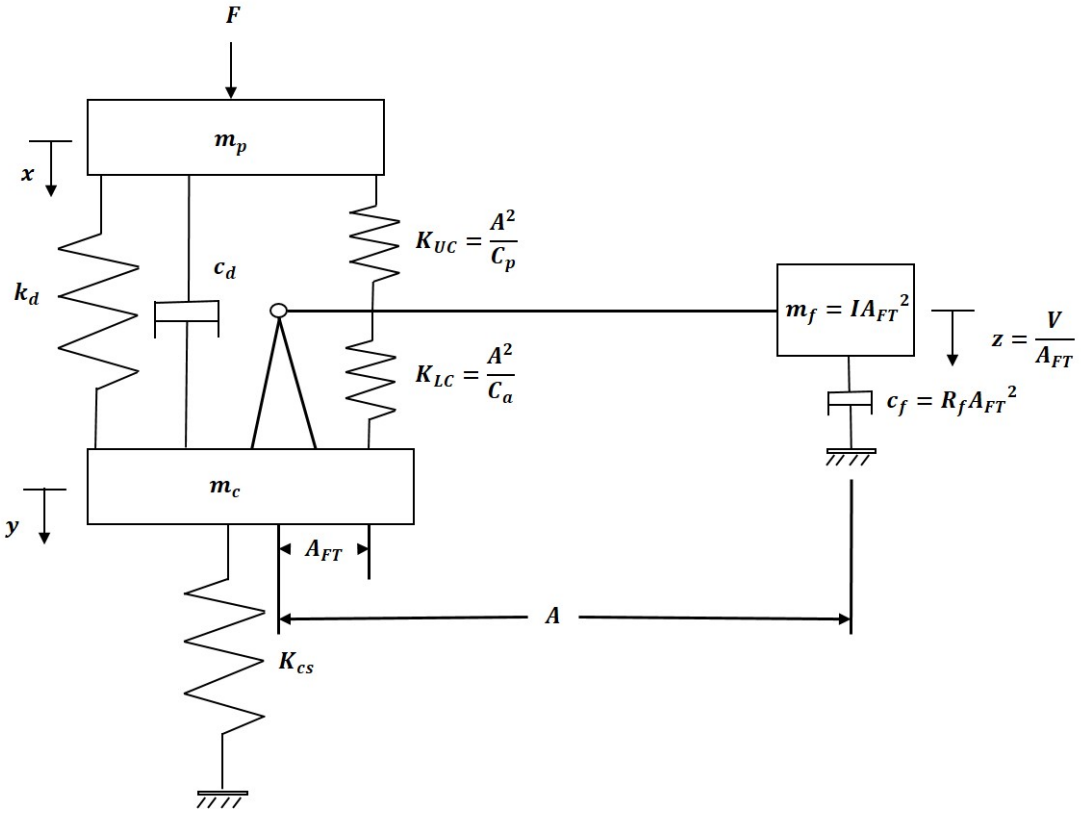

Figure 2.3: Mechanical analogy for the fluidic pitch link.

equations of motion for the FPL rotor are

$$[M]\begin{bmatrix}\overset{**}{\beta}\\ \overset{**}{\theta}\\ \overset{**}{\overline{y}}\\ \overset{**}{\overline{V}}\end{bmatrix} + [C]\begin{bmatrix}\overset{*}{\beta}\\ \overset{*}{\theta}\\ \overset{*}{\overline{y}}\\ \overset{*}{\overline{V}}\end{bmatrix} + [K]\begin{bmatrix}\beta\\ \theta\\ \overline{y}\\ \overline{V}\end{bmatrix} = \begin{bmatrix}0\\0\\0\\0\end{bmatrix}. \tag{2.9}$$

The terms of the generalized mass, damping, and stiffness matrices are shown in Eqs. (A.8–A.32). Moment equations are non-dimensionalized by the flap inertia and rotor speed squared ($I_b\Omega^2$). Time is non-dimensionalized by rotor speed such

that the non-dimensional derivatives are

$$\overset{*}{(\,)} = \frac{\dot{(\,)}}{\Omega}. \tag{2.10}$$

The displacement of the bottom of the FPL and the volume displaced into the inertia track are non-dimensionalized by the rotor radius and the rotor radius cubed, respectively. The relationship of the stiffnesses for a spring element pitch link is shown in Eq. (A.33). This will be the baseline case. The term K_θ refers to the pitch spring stiffness and is related to the pitch link stiffness, K_{pl}, and the control system stiffness, K_{cs}. The helicopter properties, which are representative of a medium duty helicopter, and FPL properties, descriptions, and values are listed in Table 2.1. These properties are similar to those used in [85, 86].

The seven properties not listed are subject to a parametric study and are: center-of-gravity (CG) offset, which is the distance from the CG of the blade to the feathering axis and is often expressed as a percentage of the chord $\left(\frac{x_I}{c}\right)$; elastomer stiffness, k_d; fluid inertance, I; piston area, A; fluid resistance, R_f; the capacitance in the upper chamber, C_p; and the accumulator capacitance, C_a.

Table 2.1: Helicopter and Fluidic Pitch Link Properties

Property	English (Metric)
Feathering Inertia, I_f, for 0% CG Offset	1.51 slug-ft^2 (2.05 kg-m^2)
Flap Inertia, I_b	1514 slug-ft^2(2052 kg-m^2)
Chord, c	1.73 ft (0.527 m)
Radius, R	26.8 ft (8.17 m)
Mass of the Piston, m_p	0.03 slugs (0.438 kg)
Mass of the Outer Can, m_c	0.06 slugs (0.876 kg)
Pitch Horn Length, l_{ph}	0.6 ft (0.183 m)
Mass of the Blade, m_b	0.236 slugs/ft (11.3 kg/m)
Elastomer Damping, c_d	15 lb-s/ft (2.05 N-s/m)
Flap Spring Stiffness, K_β	1.14×10^6 lb-ft/rad (1.55×10^6 N-m/rad)
Pitch Link Spring Stiffness, K_{pl}	1.78×10^6 lb/ft (26×10^6 N/m)
Control System Stiffness, K_{cs}	6.29×10^4 lb/ft (9.18×10^5 N/m)
Rotor Speed, Ω	27 rad/s
Lock Number, γ	6.5344
Loewy's Lift Deficiency Function, C'	1

2.3 Stability Analysis

The baseline for comparison of the FPL rotor is a simple spring element for the pitch link and rotor with a 0% CG offset. The helicopter parameters are representative of a medium duty helicopter. The baseline model can be numerically obtained from Eq. (2.9) by setting k_d to numeric infinity and C_p to an infinitesimal number.

Eq. (A.34) demonstrates how to put general mass, damping, and stiffness matrices into first order form. $\underline{0}$ and $\underline{I}$ are the zero and identity matrices, respectively, of the same dimension as the generalized mass, damping, and stiffness matrices.

For the hover cases, the advance ratio is zero and thus the periodic coefficients will become zero and leave a constant coefficient $[A]$. The eigenvalues of this matrix can then be easily calculated using any standard eigenanalysis routine such as

the "`damp.m`" command in MATLAB, which can be used to find the eigenvalues, damping ratios, and natural frequencies of any first order system matrix.

In the general case of Eq. (2.9), there are periodic coefficients in $[A]$, so Floquet Theory is used to obtain stability results. The Floquet Transition Matrix, $[\Phi(T,0)]$, relates the values of the state variables at the beginning and end of the period [96].

The Floquet Transition Matrix can be calculated in a variety of ways. Two numerical methods are demonstrated in [97]: Hsu's method and a fourth order Runge-Kutta-Gill method. Hsu's method was faster in this case and is again presented here for convenience. First, divide each period into K intervals denoted by ψ_k where $k = 0, 1, 2, ..., K$. $\psi_0 = 0, ..., \psi_K = T$ with equal intervals $h = \psi_k - \psi_{k-1}$. In the k^{th} interval, $[A(\psi)]$ is replaced by a constant matrix, $[C_k]$, such that

$$[C_k] = \frac{1}{h}\int_{\psi_{k-1}}^{\psi_k} [A(\xi)]\, d\xi. \tag{2.11}$$

Then the theory of linear differential equations with constant coefficients allows the Floquet Transition Matrix to be approximated by

$$[\Phi(T;K)] \approx e^{\psi_K - \psi_{K-1}[C_K]} e^{\psi_{K-1} - \psi_{K-2}[C_{K-1}]} \cdots e^{\psi_1 - \psi_0[C_1]} \tag{2.12}$$

or

$$[\Phi(T;K)] \approx \prod_{i=1}^{K} e^{h[C_i]}. \tag{2.13}$$

where $[C_i] = \left[C_{k|_{K-(i-1)}}\right]$. Friedmann's paper also notes that the matrix exponential can be approximated by another series. However, MATLAB has an efficient function for approximating the matrix exponential in "`expm.m`".

The eigenvalues of the Floquet Transition matrix are termed the characteric multipliers, Λ_i. The characteristic exponents, λ_i, are related to the characteristic

multipliers by

$$e^{\lambda T} = \Lambda \tag{2.14}$$

where $T = 2\pi$, in this case, is the period of the system. The stability can be analyzed using either the characteristic multipliers or the characteristic exponents. The system is stable if the absolute values of all real parts of the characteristic multipliers are less than one or equivalently if the real parts of all characteristic multipliers are less than zero [98].

The distance from the negative real part of a complex eigenvalue or characteristic exponent, λ, to the imaginary axis in the complex plane,

$$-\,Re\,(\lambda) = \sigma = \frac{\zeta\omega_n}{\Omega}, \tag{2.15}$$

is termed the stability margin and denoted σ for the remainder of this paper. ζ is the damping ratio and ω_n is the natural frequency.

2.4 Parameter Study Results

By using the parameters established in Table 2.1, the baseline helicopter properties are enumerated in Table 2.2. The objective of the parameter study is to analyze the stability margin, particularly for rotors with the FPL and various CG offsets (positive aft). As the CG offset shifts aft, the pitch natural frequency reduces. In order to maintain the baseline pitch natural frequency of 4.5/rev, the pitch inertia in the baseline model is reduced with the CG offset. Accordingly, the new pitch inertia values are used in the FPL rotor model for calculations. Table A.1 displays I_f^* values for integer values of CG offset from 0 to 12%. A parameter study explored the stability of rotors with FPLs in hover. Select results were also analyzed for

forward flight stability.

Table 2.2: Baseline Helicopter Properties

Property	Value
Flap Damping Ratio, ζ_β	0.398
Flap Natural Frequency, ω_β/Ω	1.028/rev
Flap Stability Margin, σ_β	0.409
Pitch Damping Ratio, ζ_θ	0.0923
Pitch Natural Frequency, ω_θ/Ω	4.50/rev
Pitch Stability Margin, σ_θ	0.415

2.4.1 Hover

Positive stability results were found for a variety of parameter combinations during the study. One common feature of FPL rotor designs with a stability margin comparable to or larger than the baseline is a high fluid resistance, which should be tuned to maximize the pitch stability margin. One such case is illustrated in Figure 2.4. In this instance with a 5% CG offset, the stability margin for pitch is maximized at a fluidic resistance equal to 7.15×10^8 Pa-s/m^3 (4.23×10^5 lb-s/ft^5) and a stability margin of 0.489, which is greater than the rigid baseline case. The FPL parameters are listed in Table 2.3. The corresponding natural frequencies and damping ratios for Figure 2.4 are shown in Figure 2.5 and Figure 2.6, respectively. The peak in the stability margin for pitch occurs due to the peak in the damping ratio, which overcomes the slight decrease in natural frequency as the resistance approaches 10^9 Pa-s/m^3.

Using the same parameters and fixing resistance at 7.15×10^8 Pa-s/m^3 (4.23×10^5 lb-s/ft^5), the variation of stability margin with CG offset for the pitch and flap modes of the baseline and FPL rotor configurations is illustrated in Figure 2.7. The variation of stability margin with CG offset demonstrates that the FPL rotor can

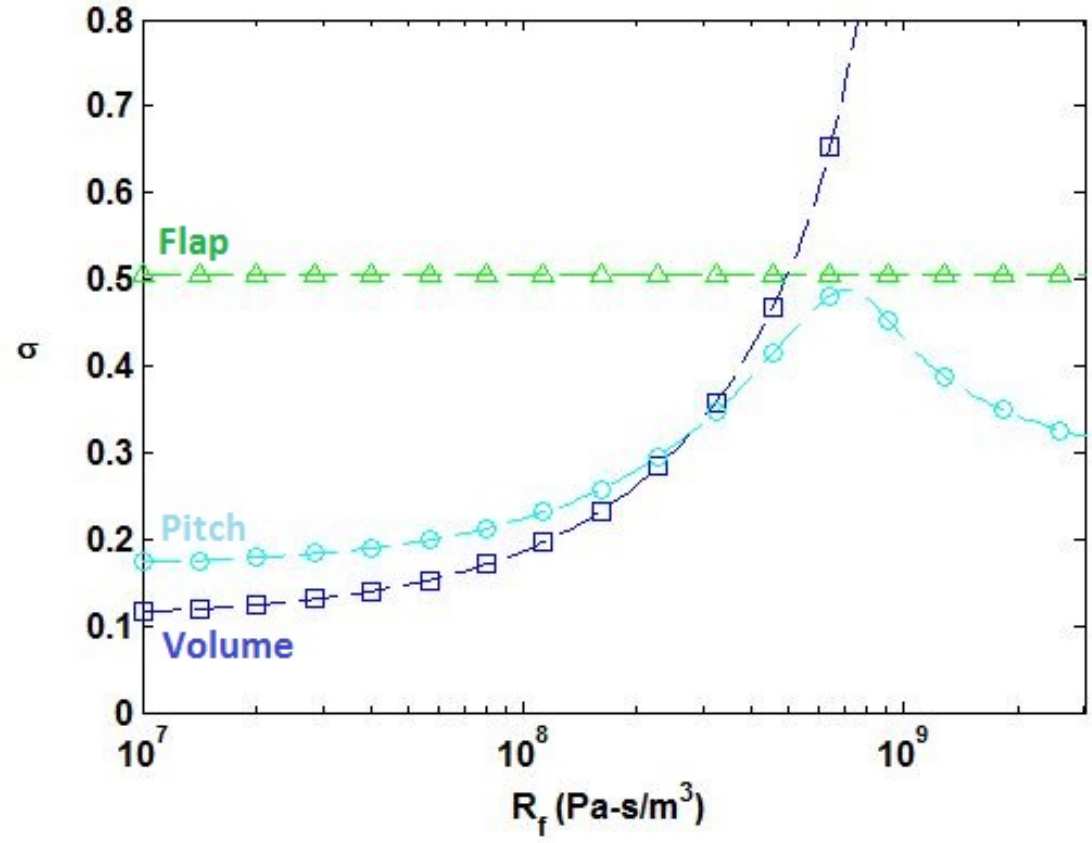

Figure 2.4: Stability margins of the first three modes versus fluid resistance for FPL rotor configuration at a 5% CG offset.

maintain the same or greater stability margin as the baseline case with 0% CG offset until approximately 8% CG offset. It also retains a large stability margin at 12% CG offset whereas the baseline goes unstable at approximately 11.6% CG offset as encapsulated in Figure 2.7. The FPL parameters are listed in Table 2.3. The equation for the damping ratio of the FPL is

$$\zeta_{FPL} = \frac{R_f}{2}\sqrt{\frac{C_a C_p}{I\left(C_a + C_p\right)}}. \tag{2.16}$$

The damping ratio for this FPL is 13.4%. The equation for the static stiffness of

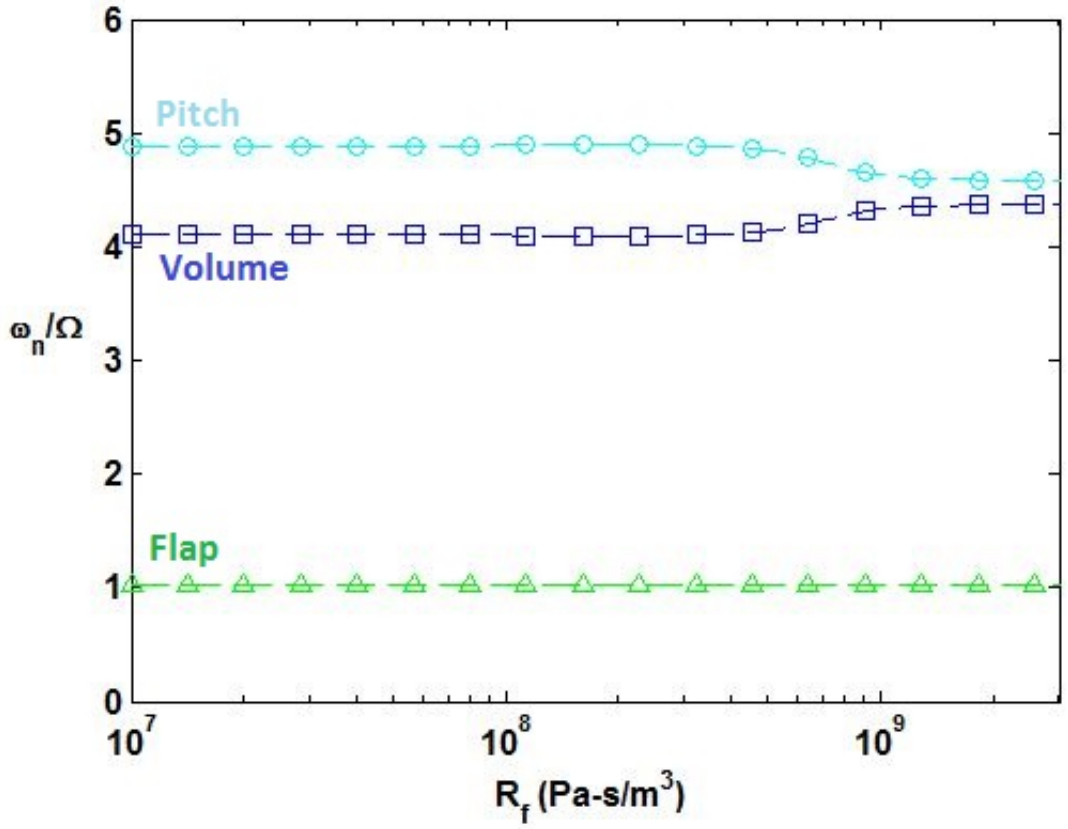

Figure 2.5: Natural frequencies of the first three modes versus fluid resistance for FPL rotor configuration at a 5% CG offset.

the FPL is

$$k_{ss} = k_d + \frac{A^2}{C_a + C_p}. \tag{2.17}$$

The static stiffness is dominated by the elastomer stiffness for high stiffness values. In this case, the static stiffness is 22.5×10^6 N/m (1.54×10^6 lb/ft) and the elastomer stiffness makes up nearly 98% of the static stiffness.

While the static stiffness in the last example was dominated by the elastomer stiffness, an example in which the elastomer stiffness is smaller and thus the static stiffness is more heavily impacted by the capacitance terms is illustrated in Figure 2.8. The FPL parameters for these curves are listed in Table 2.4. The static

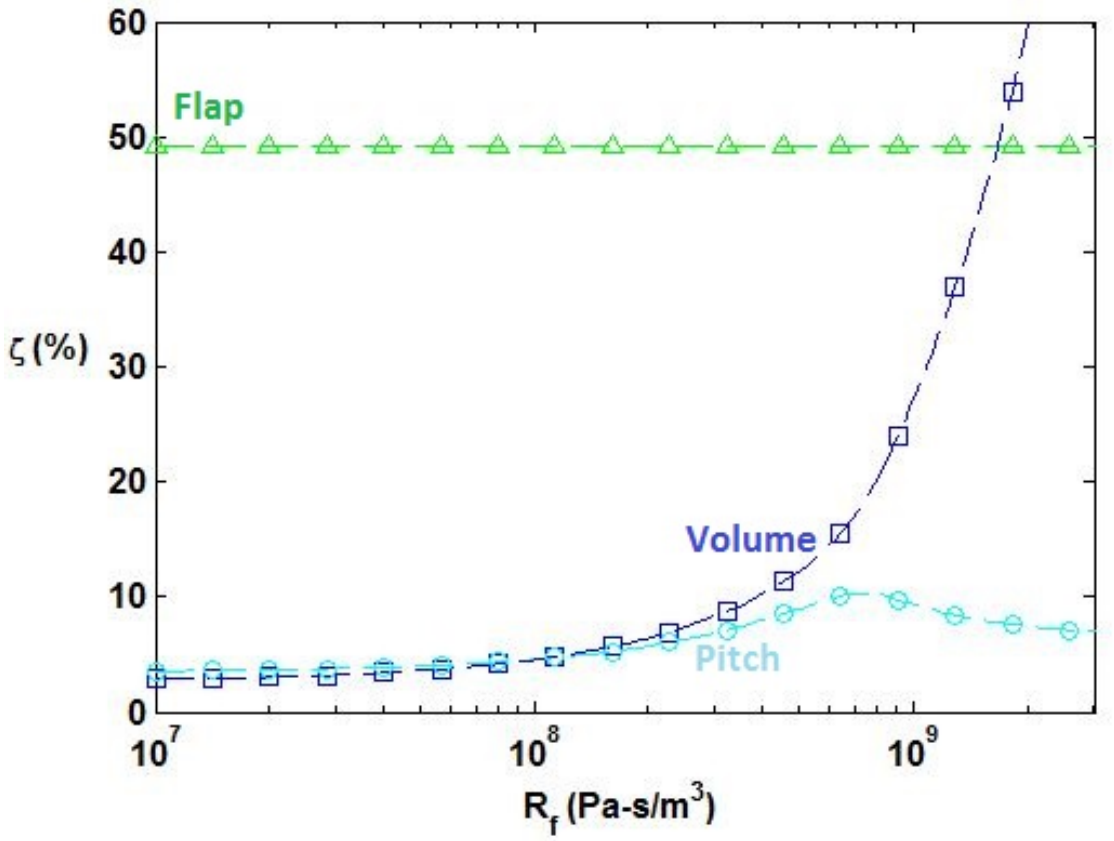

Figure 2.6: Damping ratios of the the first three modes versus fluid resistance for FPL rotor configuration at a 5% CG offset.

stiffness values for the FPL rotor configurations are 5.37×10^5 N/m (3.68×10^4 lb/ft), 1.10×10^6 N/m (7.54×10^4 lb/ft), and 6.78×10^6 N/m (4.65×10^5 lb/ft) making up 11.7%, 57.7%, and 93% of the static stiffness, respectively. As the capacitance values increase, the peak stability margin occurs at a further aft location. This is due to the minimum stability margin coming from the flap mode until the peak capacitance. After the peak, the pitch mode dictates the minimum stability margin as can be seen in Figure 2.7.

Now looking at a specific CG offset, the capacitance is varied to see its impact on the stability margin. This is illustrated in Figure 2.9. The parameters used are the

Table 2.3: Fluidic Pitch Link Properties for Figures 2.4–2.7

Property	English	Metric
k_d	1.51×10^{6} lb/ft	22×10^{6} N/m
A	0.097 ft^2	0.009 m^2
I	8220 slugs/ft^4	1.39×10^{7} kg/m^4
C_p	1.37×10^{-9} ft^5/lb	1.6×10^{-12} m^5/N
C_a	1.37×10^{-7} ft^5/lb	1.6×10^{-10} m^5/N
R_f	4.23×10^{5} lb-s/ft^5	7.15×10^{8} Pa-s/m^3

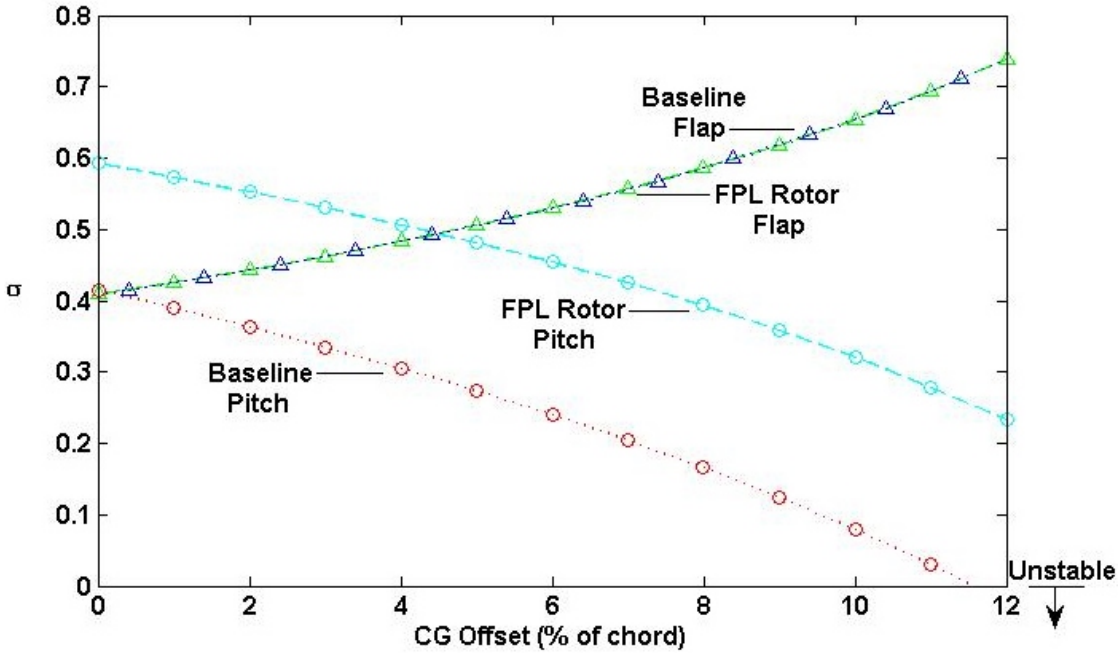

Figure 2.7: Stability margins versus CG offset of the pitch (circles) and flap (triangles) modes for baseline (dotted) and FPL rotor (dashed) configurations.

same as in Table 2.4 except that a CG offset of 6% is specified while capacitance is being varied. For very low capacitance values, the rigid pitch link case is recovered. Interestingly enough, the configuration with increased CG offset needs a lower capacitance value to match the rigid pitch link than with 6% CG offset. The higher CG offset case also shows a peak in stability margin at 0.546 for $C_p = 6.44 \times 10^{-14}$ m^5/N (1.09 ft^5/lb) that does not show up when the CG is located at the quarter

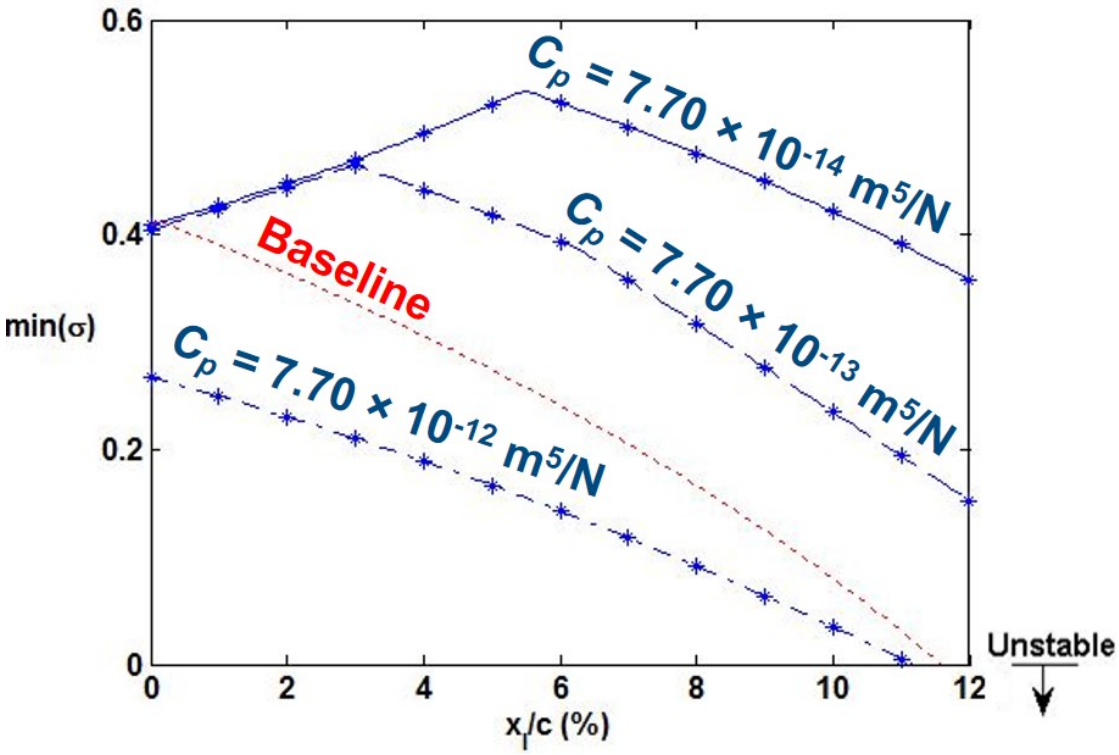

Figure 2.8: Stability margins of the baseline (red dotted) and FPL with varying capacitance at 6% CG offset (blue) rotor configurations. C_{p1} is dot-dashed, C_{p2} is dashed, and C_{p3} is solid.

chord.

Table 2.4: Fluidic Pitch Link Properties for Figure 2.8

Property	English	Metric
k_d	3.25×10^4 lb/ft	4.74×10^5 N/m
A	0.075 ft^2	0.007 m^2
I	7040 slugs/ft^4	1.19×10^7 kg/m^4
C_{p1}	1.30×10^{-8} ft^5/lb	7.70×10^{-12} m^5/N
C_{p2}	1.30×10^{-9} ft^5/lb	7.70×10^{-13} m^5/N
C_{p3}	1.30×10^{-10} ft^5/lb	7.70×10^{-14} m^5/N
C_a	$100C_p$	$100C_p$

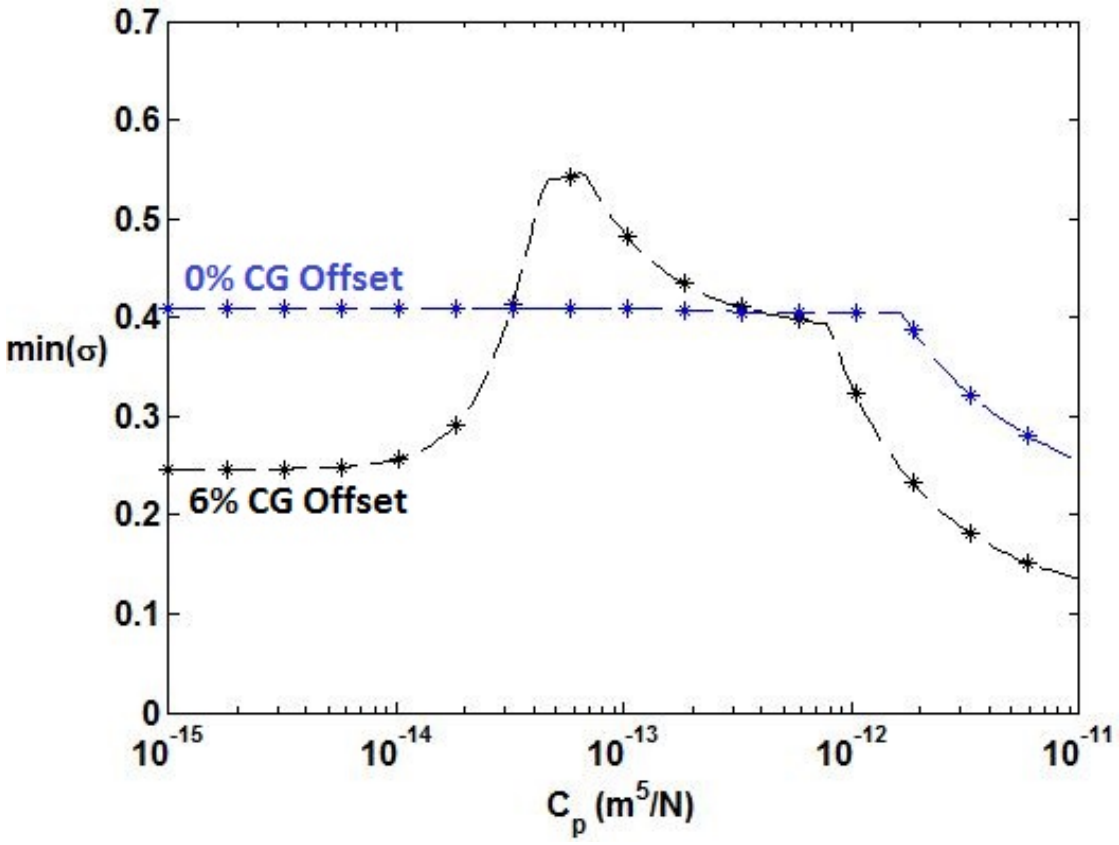

Figure 2.9: Stability margins of the FPL rotor for varying capacitance in the upper chamber and fixed CG at 0% (blue) and 6% (black) offset.

2.4.2 Forward Flight

The objective of the forward flight analysis was to examine if the FPL parameters had any adverse affect on stability margin by looking at several good hover designs and sweeping the advance ratio from 0 to 0.35. Since the objective was to look for any adverse affects created by the FPL parameters, Theodorsen's lift deficiency function, C, was assumed to be 1 for simplicity. Two examples of the stability of FPL rotor configurations in forward flight are illustrated in Figures 2.10 and 2.11. The FPL parameters are the same as in Tables 2.3 and 2.4, respectively. These two cases are representative of the parameter study. While the FPL can provide a positive or negative influence on the slope of the minimum stability margin versus advance ratio curves in forward flight, the FPL rotor configurations observed a marked improvement in stability margin above the baseline rigid pitch link over the entire range of advance ratios of interest. The result in Figure 2.10 is particularly interesting as it shows a slightly positive slope for the minimum stability margin over the entire range of advance ratios.

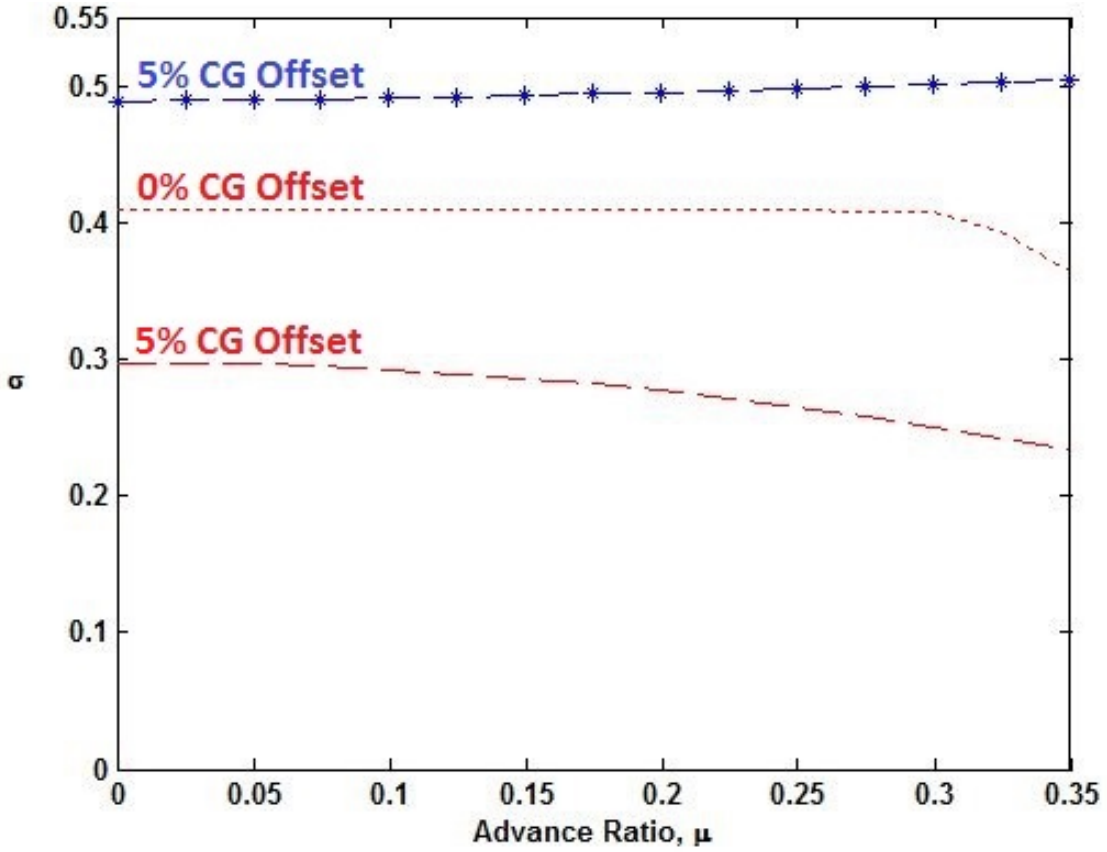

Figure 2.10: Stability margins of an FPL rotor with 5% CG offset in forward flight compared with the baseline rotor for two CG offsets, 0% and 5%.

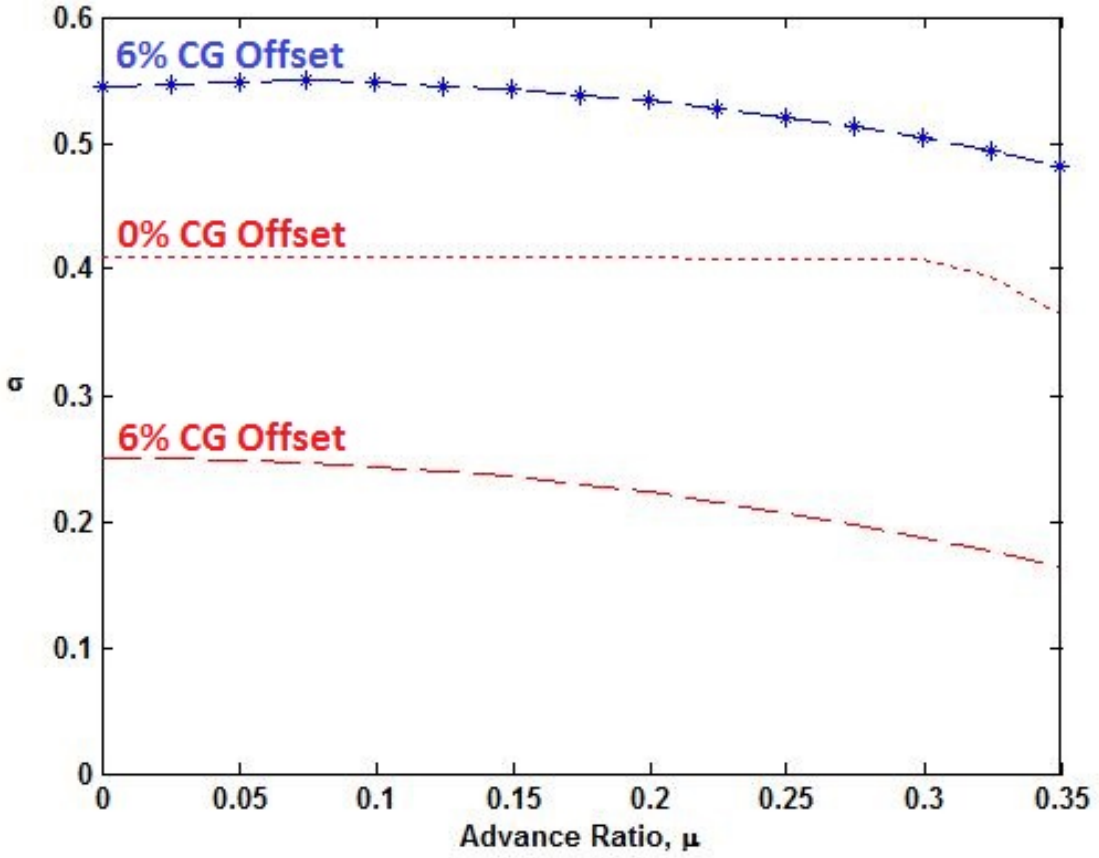

Figure 2.11: Stability margins of an FPL rotor with 6% CG offset in forward flight compared with the baseline rotor for two CG offsets, 0% and 6%.

2.5 Conclusions

1. Fluidic pitch links can be used to add damping into the pitch mode thus enabling a higher CG offset for helicopters. While the baseline case goes unstable at 12% CG offset, there are fluidic pitch link designs that retain significant stability margins under these conditions. These fluidic pitch link designs could open up the blade design space by enabling decreased leading edge weight or a redistribution of mass in blade designs that may have previously resulted in an unstable system.
2. Increasing fluidic resistance enables damping to be added into the pitch mode. Fluidic pitch link designs can show more than 10% damping added into the pitch mode. This can enable a higher CG offset for helicopter rotor blades or stabilize unstable ones.
3. Reducing capacitance for a rotor configuration with a CG offset can increase the stability margin until fluid capacitance becomes too low causing the rigid pitch link case to be recovered.
4. The positive stability margins that are found for the fluidic pitch links in hover are marginally affected by the periodic terms that appear in forward flight and the margins are better across the entire range of advance ratios.
5. Fluidic pitch links show great potential for improving hover stability or enabling blade design changes without causing an unstable condition in forward flight.

Chapter 3

Testing of the Fluidic Pitch Link Model

3.1 Introduction

The work presented in Chapter 2 examines a single pumper design of a FPL model. However, as noted by Vahdati in [99], double pumpers are more commonly used in aerospace applications due to their increased safety and reduced risk of fluid cavitation. Cavitation describes the process in which vapor-filled cavities nucleate, grow, and implode. These cavities occur in a liquid when the local static pressure of the liquid is reduced below its vapor pressure. When the cavities flow into a higher pressure region, they can implode violently thus causing very high pressure peaks, performance degradation, high vibration levels, and even erosion of surrounding materials [100].

If the top elastomer fails in a double pumper design, the top and bottom plates will still remain rigidly connected as opposed to the single pumper design, which will separate, thus increasing the safety of the double pumper design. Additionally, since

stiff elastomers are typically used in the top and bottom sections, double pumpers are more easily pressurized than single pumpers, which use a soft diaphragm in the lower chamber. This reduces the risk of cavitation in double pumper designs. Accordingly, the objective of this chapter is to experimentally validate a double pumper FPL model.

3.2 Fluidic Pitch Link Modeling

A schematic of a FPL is illustrated in Figure 3.1. There are two degrees of freedom: piston displacement, x, and volume of fluid displaced into the fluid track from equilibrium, V. The volume is not deterministic from the piston displacement due to the compressibility in the fluid and bulging of the elastomer. The elastomer sections act as parallel springs and dampers with axial stiffnesses, $k_d/2$, and damping coefficients, $c_d/2$, respectively. The top and bottom fluid chambers have capacitances C_t and C_b, respectively. The fluid track has cross-sectional area, A_{FT}; fluid resistance, R_f; and inertance, I. The inertance is defined as

$$I = \frac{\rho L}{A_{FT}}, \tag{3.1}$$

where ρ is the fluid density and L is the fluid track length. The pitch link body has mass, m_c. The equations for the mechanical-fluidic coupling are

$$p_t = \frac{1}{C_t}\left[Ax - V\right] \tag{3.2}$$

and

$$p_b = \frac{1}{C_b}\left[V - Ax\right]. \tag{3.3}$$

A is the cross-sectional area of the piston. The equation for the fluid flow through the fluid track is

$$p_t - p_b = I\ddot{V} + R_f\dot{V}. \tag{3.4}$$

Eqs. (3.2–3.3) can then be substituted into Eq. (3.4) in order to determine the first equation of motion,

$$I\ddot{V} + R_f\dot{V} + \left(\frac{1}{C_t} + \frac{1}{C_b}\right)V - A\left(\frac{1}{C_t} + \frac{1}{C_b}\right)x = 0. \tag{3.5}$$

The second equation of motion can be found by summing the forces on the piston,

$$m_p\ddot{x} + c_d\dot{x} + \left[A^2\left(\frac{1}{C_t} + \frac{1}{C_b}\right) + k_d\right]x - A\left(\frac{1}{C_t} + \frac{1}{C_b}\right)V = F. \tag{3.6}$$

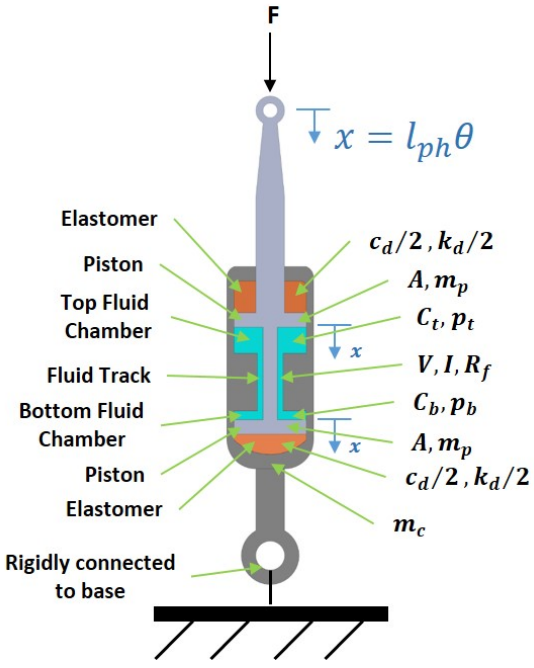

Figure 3.1: Model of a double pumper fluidic pitch link.

Additionally, the equivalent mechanical model of this system can be derived

and is illustrated in Figure 3.2. The vertical displacement of the fluid in the fluid track, z, is related to the volume of fluid displaced from equilibrium, V, by

$$z = \frac{V}{A_{FT}}. \tag{3.7}$$

The fluid resistance, R_f, can be represented by a dashpot, c_f, where

$$c_f = R_f A_{FT}^2. \tag{3.8}$$

The inertance, I, can be represented by a mass, m_f, where

$$m_f = I A_{FT}^2. \tag{3.9}$$

The capacitances in the top and bottom chambers, C_t and C_b, respectively, can be treated as springs related to the piston area by

$$K_t = \frac{A^2}{C_t} \tag{3.10}$$

and

$$K_b = \frac{A^2}{C_b}. \tag{3.11}$$

3.2.1 Nondimensionalization

The non-dimensionalization scheme follows from the work completed in Chapter 2 and Treacy et al. [101]. Multiply Eq. 3.5 by R^2 where R is a rotor radius. Then

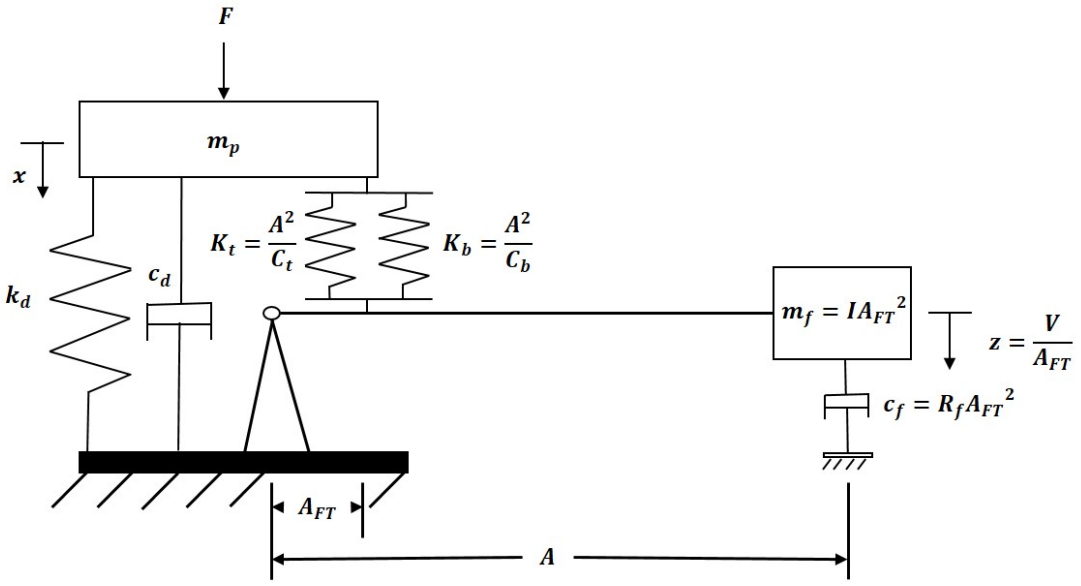

Figure 3.2: Mechanical model of a double pumper fluidic pitch link.

divide the resulting equation and Eq. 3.6 by $m_b\Omega^2R^2$ to obtain

$$\begin{bmatrix} \overline{I} & 0 \\ 0 & \overline{m}_p \end{bmatrix} \begin{bmatrix} \overline{V}^{**} \\ \overline{x}^{**} \end{bmatrix} + \begin{bmatrix} \overline{R}_f & 0 \\ 0 & \overline{c}_d \end{bmatrix} \begin{bmatrix} \overline{V}^{*} \\ \overline{x}^{*} \end{bmatrix} + \begin{bmatrix} \overline{k}_1 & -\overline{k}_{12} \\ -\overline{k}_{12} & \overline{k}_2 \end{bmatrix} \begin{bmatrix} \overline{V} \\ \overline{x} \end{bmatrix} = \begin{bmatrix} 0 \\ \overline{F} \end{bmatrix}. \tag{3.12}$$

The bars indicate a non-dimensionalized parameter. The mass per unit span of a rotor blade is m_b while Ω is the blade rotation frequency. Note that m_p is a mass while m_b is a mass per unit length. The piston displacement, x, and volume of fluid displaced from equilibrium in the fluid track, V, are non-dimensionalized by R and R^3, respectively, such that

$$\overline{x} = \frac{x}{R}, \tag{3.13}$$

$$\overline{V} = \frac{V}{R^3}. \tag{3.14}$$

The non-dimensional derivatives are given by

$$(\overset{*}{\ }) = \frac{(\dot{\ })}{\Omega}. \tag{3.15}$$

All of the non-dimensional parameters are given in the Appendix as Eqs. (B.1–B.12).

3.3 Test Setup

A FPL was designed, manufactured, and tested at LORD Corporation in order to obtain the veracity of the FPL model. In particular, a new swappable fluid track design has been created to allow multiple track lengths to be tested. Please keep in mind that the external fluid track is for prototype purposes to enable flexibility in circuit design for interchanging the fluid track. A typical production level design makes use of an internal fluid track. However, an external fluid track has been demonstrated in a LIVE pylon mount for the Bell 505 Jet Ranger X [102] and could be integrated into a production level design if it were beneficial to the performance or design of a FPL. Four circuits were tested and CAD models of each are illustrated in Figures 3.3–3.4. An additional feature of this model, two pressure transducers are attached to obtain the pressure difference between the top and bottom fluid chambers. A cross-section of the CAD model with components labeled is illustrated in Figure 3.5.

A CAD model of the fluid track design with circuit 1 attached is illustrated in Figure 3.6. The top and bottom faces of this part contact the fluid in the top and bottom chambers of the fludic pitch link. Large slots on the top and bottom faces have been milled to minimize the resistance of the fluid flow through the fluid track. SAE o-ring bosses enable fluid to flow radially into and out of the part. These

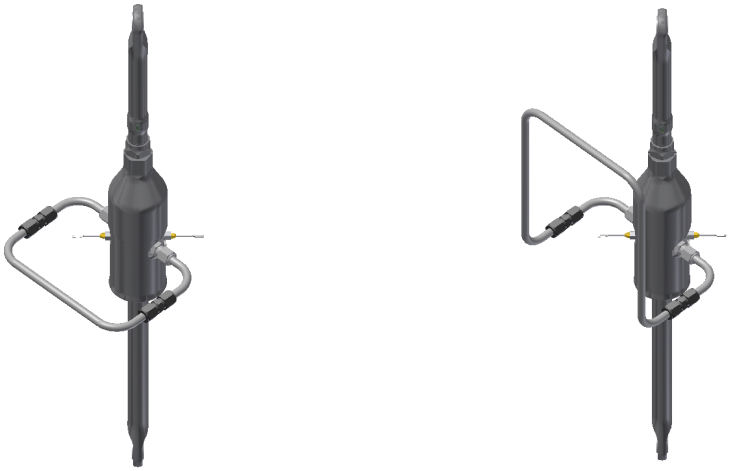

Figure 3.3: CAD models of fluidic pitch links with circuit 1 (left) and circuit 2 (right).

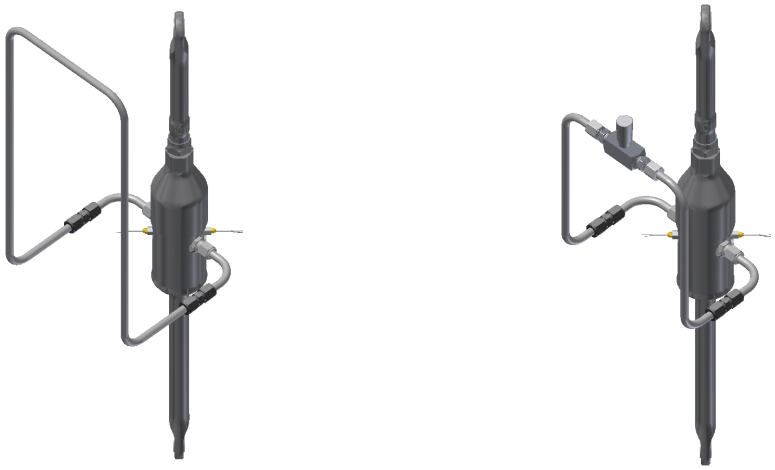

Figure 3.4: CAD models of fluidic pitch links with circuit 3 (left) and circuit 4 (right).

features are illustrated in the CAD models shown in Figures 3.7–3.8. A Parker Ferulok® adapter is used to connect the SAE port to the tubing via compression fitting. An adapter connects the pressure transducers to the machined slots in order to record the pressure in the two fluid chambers. After a 90° bend, a union

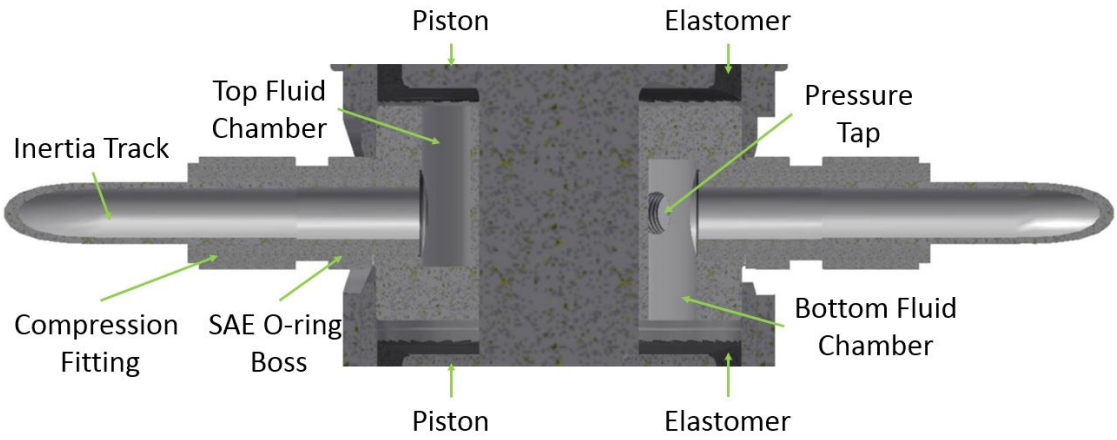

Figure 3.5: CAD model of a fluidic pitch link cross-section.

with compression fittings on both ends enables swapping of the tubing to test the varying tubing lengths.

Systematic tubing length changes between circuits 1-3 provide three different inertance values, which shift the natural frequencies of the system. The fourth circuit (Figure 3.4b) has an additional needle valve component. The needle valve was used to increase the resistance, which reduces the amplitudes at the notch and peak frequencies.

Each of the four circuit designs was tested at LORD Corporation in an MTS single-axis test machine as pictured in Figure 3.9. The bottom of the fluidic pitch link is fixed while the top can be hydraulically displaced to meet given force or displacement criteria. For a dynamic stiffness test, the fluidic pitch link is cycled for ten seconds at a given frequency and displacement amplitude and data is recorded during the final four seconds. The recorded force amplitude and displacement amplitude are then used to calculate the dynamic stiffness. During testing, in addition to recording force, displacement, and stiffness, the pressures in each chamber were recorded. The frequency sweep for each circuit was conducted by

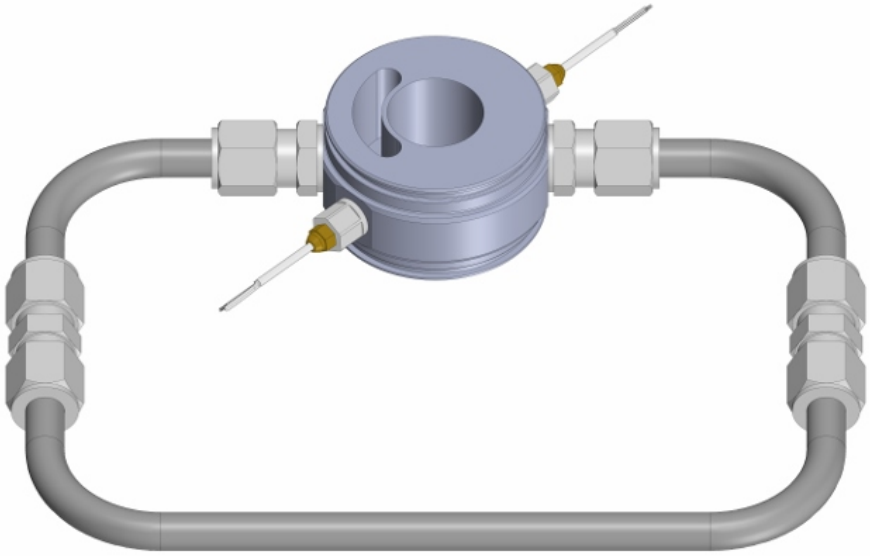

Figure 3.6: CAD model of the fluid track with circuit 1.

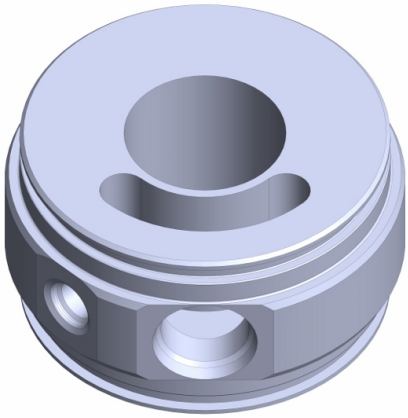

Figure 3.7: CAD model of fluid track without circuitry attached.

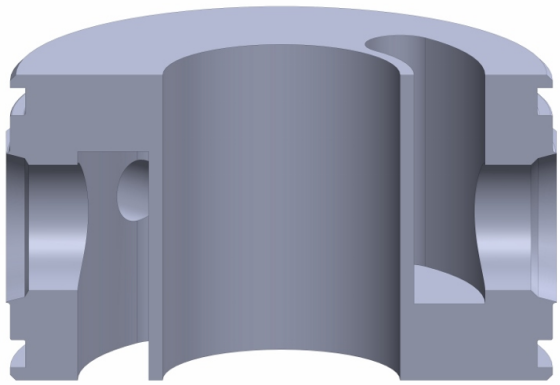

Figure 3.8: CAD model of fluid track cross-section without circuitry attached.

successively increasing frequency until the notch was captured.

3.4 Analysis Methodology

Two analysis methods were used for successfully validating the FPL model. The first method applied FPL design parameters to a simulation for comparison of the model with recorded experimental data in the time-domain and frequency-domain. This method was conducted when simulating circuits 1-3. The objective of this method was to evaluate the validity of the model to predict the experimental results. The second method utilized an empirical parameter study to match the time-domain and frequency-domain data from testing via simulation results. This method was employed for the valve closing study using circuit 4. The objective of this method was to evaluate the validity of the model to match the experimental results if the first method failed and to make note of any missing dynamics.

The empirical FPL parameters were obtained by performing a trial and error parameter study and minimizing the l^2-norm [103] of the error between the simulation

Figure 3.9: MTS single axis test at LORD Corp.

and experimental results, which is equal to

$$\|e\|_{l^2} = \sqrt{\sum_{k=1}^{n} (u_k^s - u_k^t)^2}, \tag{3.16}$$

where u represents a vector of any frequency-dependent or time-dependent variable. The superscripts s and t denote simulation and experiment, respectively. A parameter study was initiated by altering six FPL parameters and then calculating the l^2-norm of the error for the frequency response of the dynamic stiffness amplitude at the discrete test frequencies. The piston area, A; capacitance in the top chamber, C_t; capacitance in the bottom chamber, C_b; fluid resistance, R_f; elastomer stiffness, k_d; and inertance, I, were varied in order to obtain the minimum error. It was assumed that the two capacitances are equal since they derive from the same component. However, due to allowable tolerances, they are slightly different from

their nominal design value, which is expounded in the results section.

In order to simulate the model, a standard state-space respresentation is created in MATLAB using the function "`ss.m`" and the equations of motion in first order form. There is zero feedforward. The outputs are pressure in the top chamber, p_t; pressure in the bottom chamber, p_b; and displacement of the piston, x. The recorded force data from the experiment was used as an input to the MATLAB function "`lsim.m`" to calculate the time response. The frequency response was calculated by using the MATLAB function "`bode.m`" with the specified frequency vector from the corresponding circuit. To obtain the dynamic stiffness results, the amplitude from the transfer function with an input of $\overline{F}$ and output of $\overline{x}$ was inverted and the phase angle was negated. Thus the dynamic stiffness is defined as

$$\overline{K}^* = \frac{\overline{F}}{\overline{x}} = \overline{K}' + j\overline{K}'', \tag{3.17}$$

where $j = \sqrt{-1}$ is the imaginary unit. K' is the real part of the dynamic stiffness and is a measure of the FPL's stiffness. K'' is the imaginary part of the dynamic stiffness and is a measure of the FPL's damping.

Two of the FPL parameters are frequency dependent: fluid resistance, R_f, and inertance, I. These parameters are calculated at each frequency using the manner recommended by Donovan et al [104]. The equation for fluid resistance is a modification to the resistance from Poiseuille flow and, in the frequency range of interest, is equal to

$$R_f = \frac{128\mu L}{\pi D^4} 0.166\alpha^{1.49}, \alpha > 10, \tag{3.18}$$

where μ is the fluid dynamic viscosity and D is the tube inner diameter. α is a non-dimensional parameter that is a function of the frequency of oscillation, ω.

The equation for α is

$$\alpha = r_0\sqrt{\frac{\omega}{\nu}}, \tag{3.19}$$

where r_0 is the tube inner radius and ν is the fluid kinematic viscosity. Inertance is modified by multiplying Eq. 3.1 by a correction factor that is obtained from a look-up table when α is an input.

Frequency responses from the experimental results were generated by applying a discrete Fourier transform (DFT) to the time response data at each frequency using the MATLAB function "`fft.m`" to obtain the complex Fourier coefficients. The magnitude and phase can then be obtained from these coefficients by taking the absolute value and finding the angle between the real and imaginary parts, respectively. In order to obtain the correct magnitude amplitudes for a single-sided amplitude spectrum, the coefficients were normalized by the length of the signal and then non-zero frequency components were multiplied by two.

3.5 Results

Results are presented in a unique manner for each circuit to best demonstrate the multitude of comparisons that can be made. For each of circuits 1-3, frequency spectrums are reported for dynamic stiffness amplitude and the amplitude of the pressure divided by force. The results for circuit 1 additionally contain phase data for the frequency spectrums, the real part of the dynamic stiffness, and the complex part of the dynamic stiffness. The results for circuit 2 additionally include time-responses of displacement and the pressure in each chamber at a given frequency. The results for circuit 3 additionally incorporate displacement and pressure plotted against force at various frequencies. These plots are similar to

Lissajous figures [105]. Lissajous figures are a special case of parametric equations where x- and y- coordinates are written as

$$x = x_0 \sin\left(\omega_x t + \phi_x\right), \tag{3.20}$$

and

$$y = y_0 \sin\left(\omega_y t + \phi_y\right). \tag{3.21}$$

DFTs were then applied to the force, displacement, and pressure at the individual test frequencies to evaluate the effects of the magnitudes and phases from the first three harmonics. The dynamic stiffness amplitude is presented for the valve closing study at numerous valve positions to explore the effect of closing the valve on the dynamic stiffness amplitude.

The FPL parameters that were unaffected by circuit alterations and used in the simulations for circuits 1-3 are enumerated in Table 3.1

Table 3.1: Fluidic Pitch Link Properties for Circuits 1-3

Property	Value
$\overline{k}_d$	66.95
$\overline{A}$	5.103×10^{-5}
$\overline{c}_d$	8.048×10^{-2}
$\overline{C}_t$	5.267×10^{-13}
$\overline{C}_b$	5.267×10^{-13}
$\overline{m}_p$	5.814×10^{-3}
$\overline{k}_1$	1.151×10^{11}
$\overline{k}_2$	366.6
$\overline{k}_{12}$	5.872×10^{6}

The model validation was deemed successful if the simulation predicted the notch frequency within 10% of the experimental results for the range of frequencies studied, 4.1/rev–6.8/rev. The chief benefit of this model is that it provides an

excellent starting point for FPL design with a simple, low-dimensional model. In order to drastically reduce the error, significant complexity would need to be introduced.

3.5.1 Circuit 1

The non-dimensional uncorrected fluid resistance, $\overline{R}_{fu}$, is 4.237×10^6. For the remainder of the paper, all parameters are assumed to be non-dimensional unless otherwise stated. The uncorrected inertance, $\overline{I}_u$, is 4.555×10^8 as defined in dimensional form in Eq. 3.1. The equation for the dimensional uncorrected fluid resistance is

$$R_{fu} = \frac{128\mu L}{\pi D^4}. \tag{3.22}$$

The dynamic stiffness amplitude and phase frequency spectra for circuit 1 are presented in Figure 3.10. For all of the frequency responses, the solid red line is the simulation result while the blue triangles denote discrete test points. The simulation result accurately replicates the depth and location of the notch frequency. In the simulation, the notch frequency occurs at 6.8/rev while the experimental results represent the notch at approximately 6.67/rev, which is less than 2% error. However, the model breaks down at low frequency due in part to a frequency dependence of the elastomer that is unmodeled. The concave down, positive slope observed at low frequency cannot be replicated by a constant coefficient stiffness term, which can only start with a horizontal line at low frequency before beginning a concave down, negative slope due to the poles from the notch frequency. This frequency dependence can further be observed in the real and imaginary parts of the dynamic stiffness, which are illustrated in Figure 3.11 and Figure 3.12, respectively. The real part of the dynamic stiffness shows the frequency dependence of the stiffness at low

frequency. Additionally, negative stiffness that is obserbed in the real part of the dynamic stiffness after the notch frequency can be attributed to the phase shift that is illustrated in Figure 3.10b as the frequency increases. The imaginary part of the dynamic stiffness, which is a measurement of the damping in the system, reveals an even greater dependence on frequency both at low frequency due to the elastomer and throughout the frequency range due to the frequency dependence of the fluid resistance. The correction to the resistance formula is able to capture the curvature of the line, which would be straight for a constant coefficient resistance. However, the low frequency elastomer dependence is even more apparent as there is a large shift in the damping that gives the appearance of non-zero static damping even though the curve for the experiment will trend to zero if tested at small enough frequencies.

The pressure divided by force amplitude and phase frequency spectra are reported in Figure 3.13 and Figure 3.14 for the top and bottom fluid chambers, respectively. The phase has been wrapped to $\pm 180°$ for clarity. The amplitudes in both chambers match well; however, the amplitude of the pressure in each chamber differs slightly due to the variability of the capacitances in each tubeform from acceptable component tolerances that could be accounted for in the model by enabling $C_t \neq C_b$. However, this was not accounted for in this simulation since the tubeform nominal values are the same. While the amplitudes of the pressures in each chamber nearly match, the phase between each chamber varies by $180°$ as is expected from Eqs. 3.2–3.3, which shows that the pressures should be equal and opposite for $C_t = C_b$.

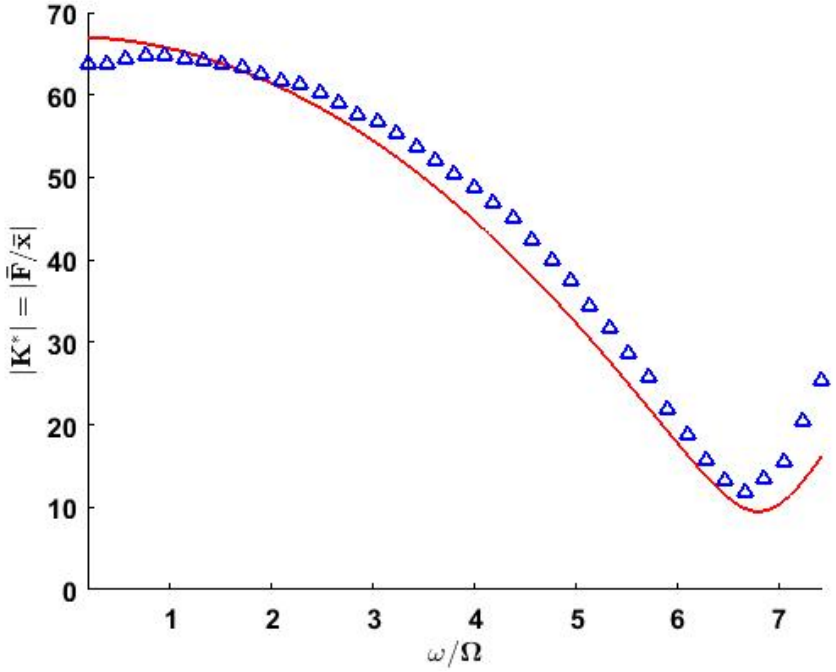

(a) Amplitude

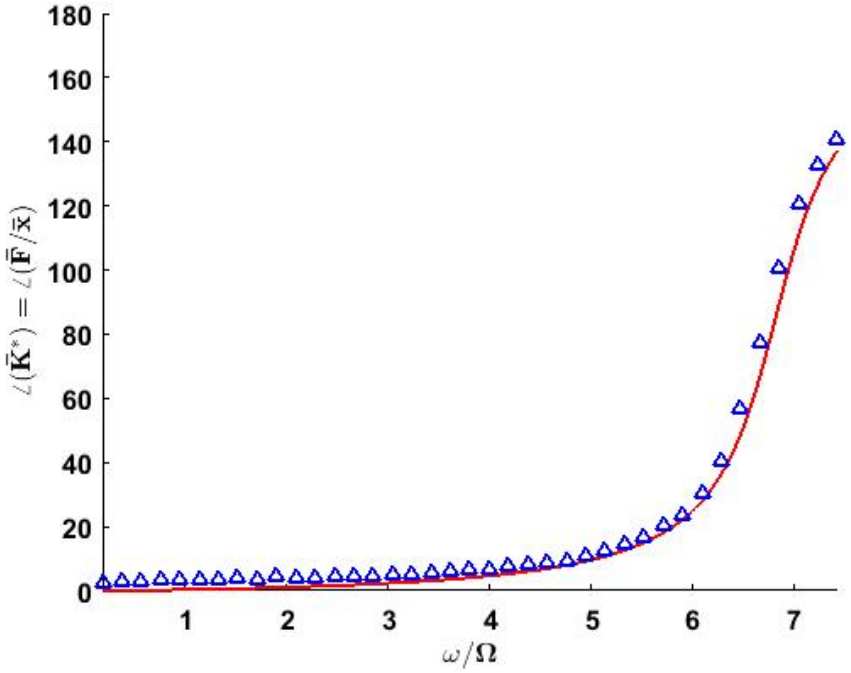

(b) Phase

Figure 3.10: Dynamic stiffness (a) amplitude and (b) phase of circuit 1. The simulation result is the red line while the experimental results are blue triangles.

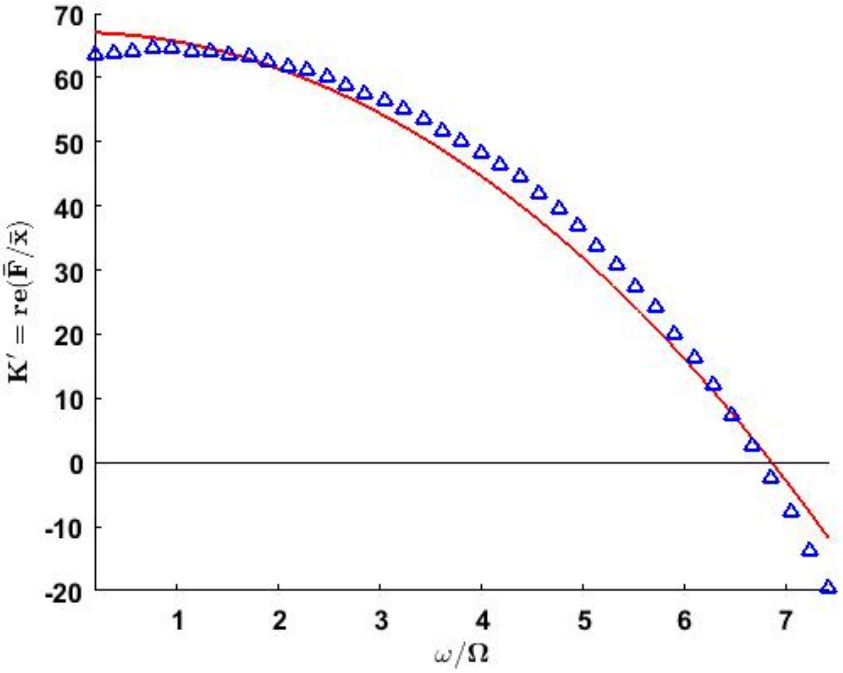

Figure 3.11: Real component of the dynamic stiffness of circuit 1. The simulation result is the red line while the experimental results are blue triangles.

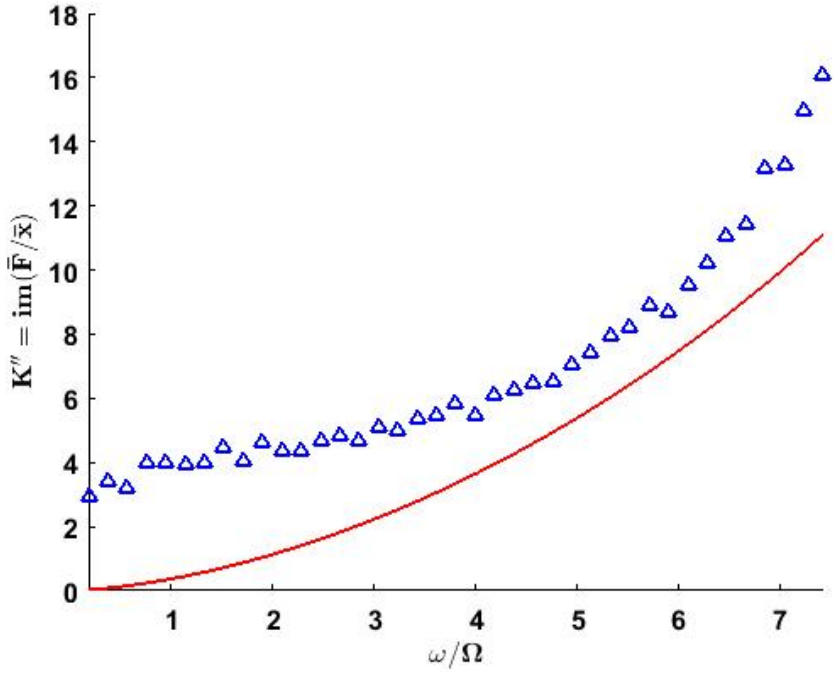

Figure 3.12: Imaginary component of the dynamic stiffness of circuit 1. The simulation result is the red line while the experimental results are blue triangles.

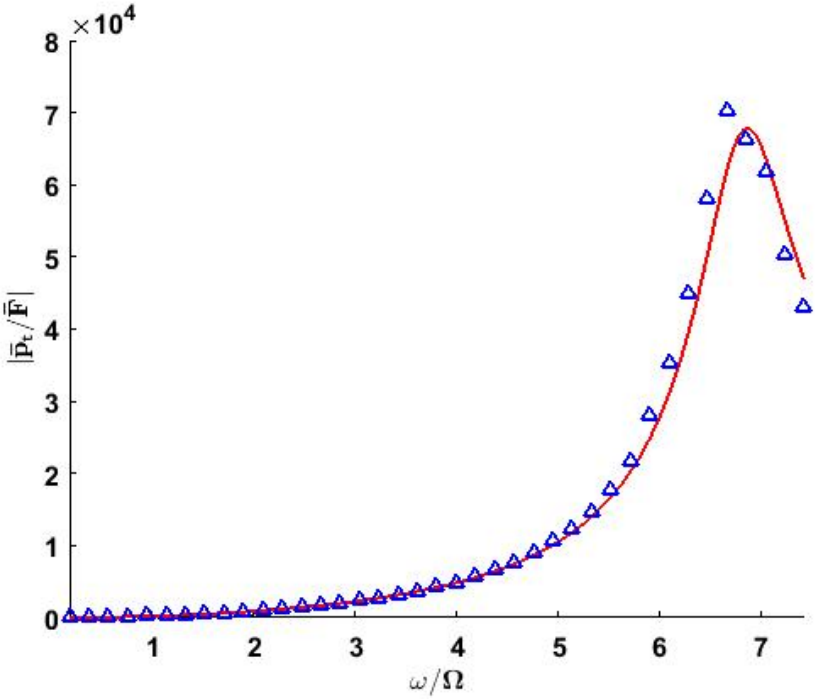

(a) Amplitude

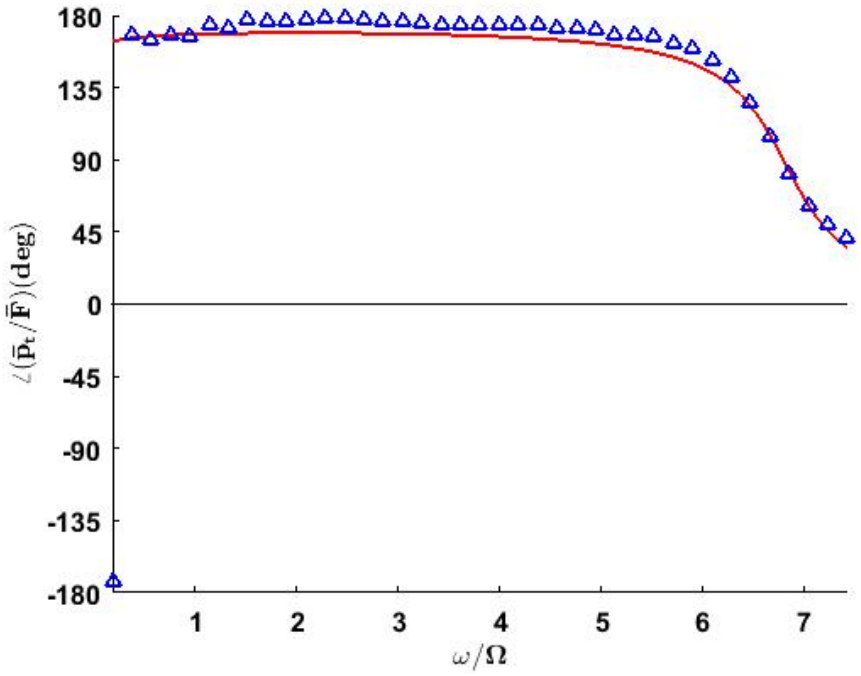

(b) Phase

Figure 3.13: (a) Amplitude and (b) phase frequency response of pressure in the top chamber divided by force for circuit 1. The simulation result is the red line while the experimental results are the blue triangles.

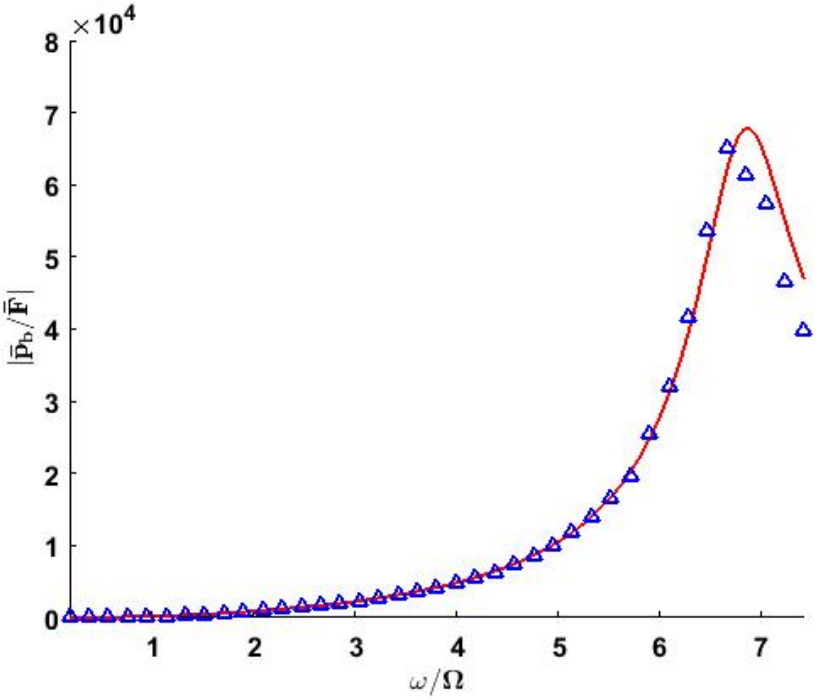

(a) Amplitude

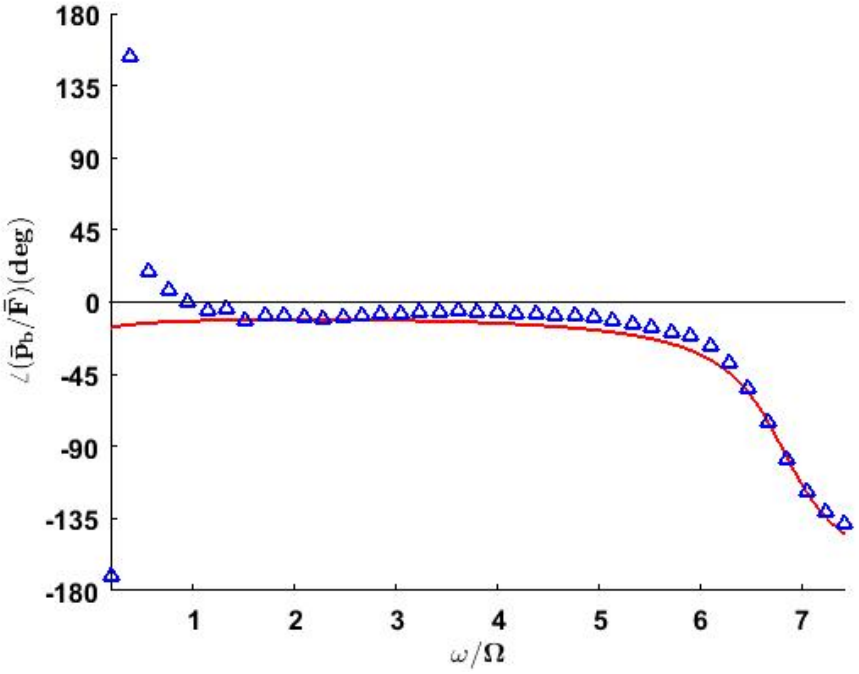

(b) Phase

Figure 3.14: (a) Amplitude and (b) phase frequency response of pressure in the bottom chamber divided by force for circuit 1. The simulation result is the red line while the experimental results are the blue triangles.

3.5.2 Circuit 2

The uncorrected fluid resistance, $\overline{R}_{fu}$, is 8.901×10^{6} and the uncorrected inertance, $\overline{I}_{u}$, is 9.570×10^{8}. The frequency spectrum for the dynamic stiffness amplitude is illustrated in Figure 3.15. With the longer fluid track, both resistance and inertance increase. Accordingly, the notch frequency shifts left and contains a slightly shallower valley than in circuit 1. The experimental notch frequency is approximately 4.85/rev while the simulation predicts that the notch frequency will occur at 4.68/rev. The error in the notch frequency location is slightly greater than in circuit 1, but it is still very good at 3.5%. Frequency spectra for the amplitudes of the pressures divided by force are illustrated in Figure 3.16 and Figure 3.17 for the top and bottom fluid chambers, respectively. The amplitude is predicted very well when accounting for the inaccuracy in the notch frequency.

As expected from the dynamic stiffness frequency response, the simulation and experimental results of the time response of the position at 0.95/rev, which is presented in Figure 3.18, match exceptionally well. The time response of the pressure in the top chamber at 3.81/rev is illustrated in Figure 3.19. The simulation overpredicts the peak pressure by 26%, which is to be expected from viewing the corresponding amplitude in the frequency spectrum from Figure 3.16. The time response of the pressure in the bottom chamber at 5.52/rev is illustrated in Figure 3.20. The simulation underpredicts the peak pressure by 8% and can similarly be expected by viewing the corresponding frequency spectrum.

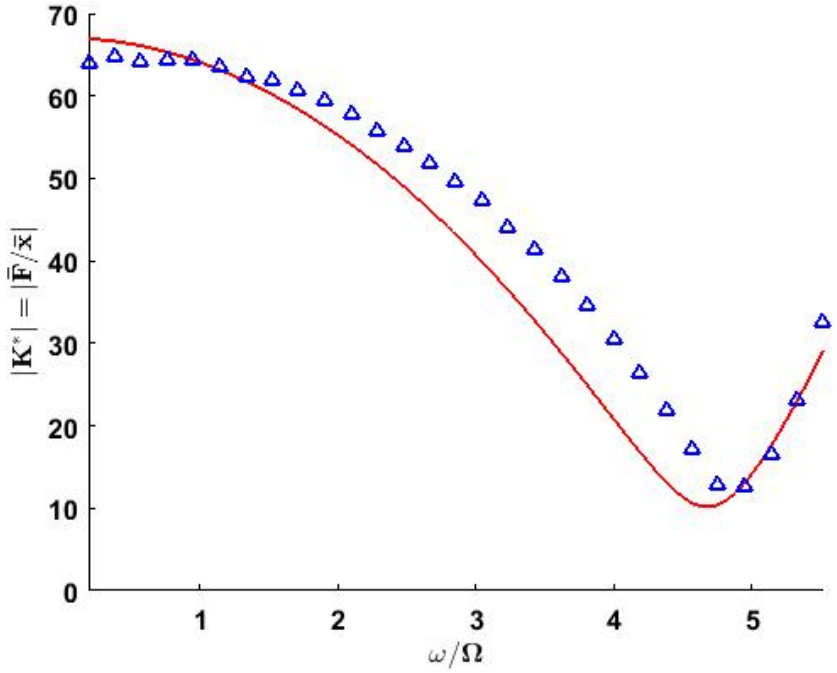

Figure 3.15: Dynamic stiffness amplitude of circuit 2. The simulation result is the red line while the experimental results are blue triangles.

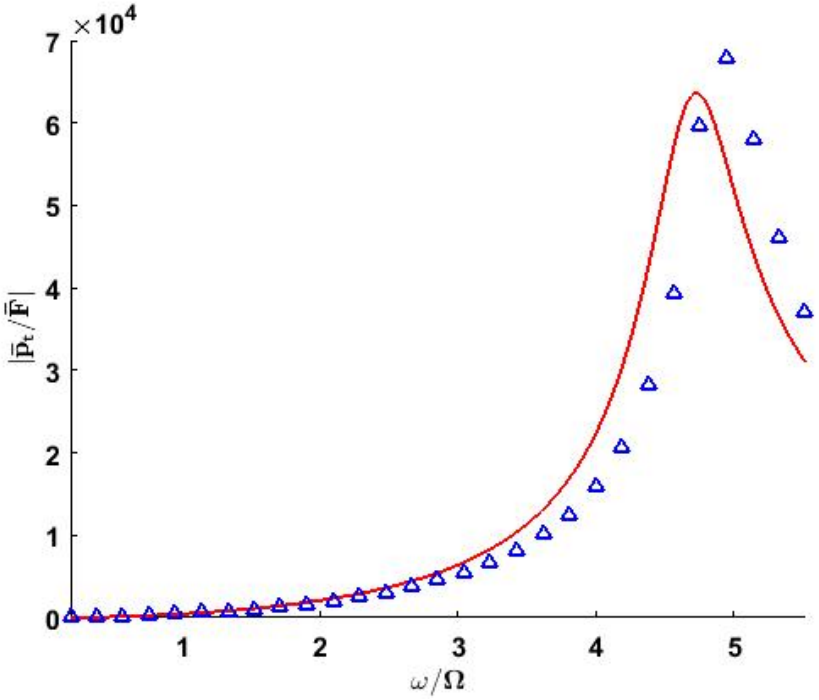

Figure 3.16: Amplitude of the pressure in the top chamber divided by force for circuit 2. The simulation result is the red line while the experimental results are blue triangles.

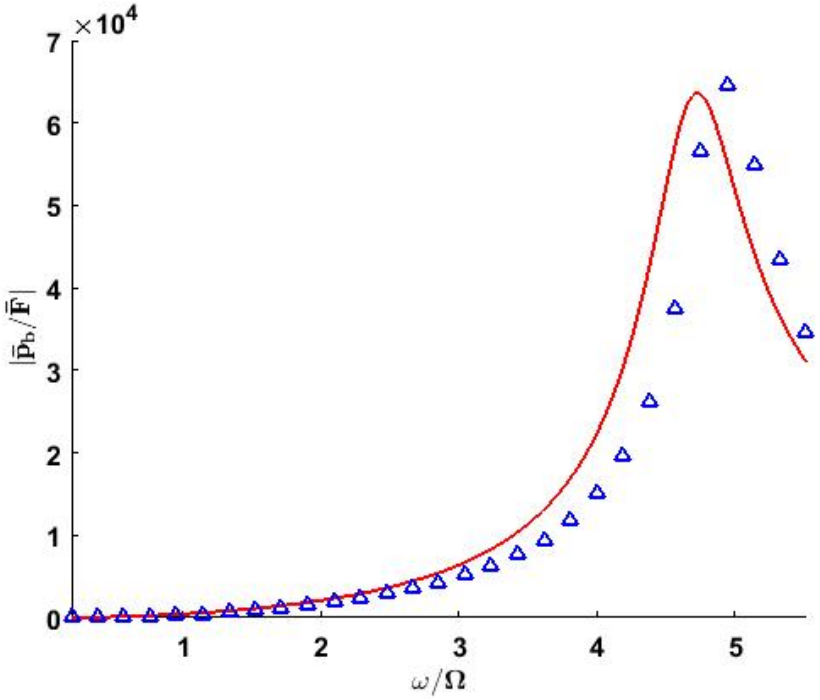

Figure 3.17: Amplitude of the pressure in the bottom chamber divided by force for circuit 2. The simulation result is the red line while the experimental results are blue triangles.

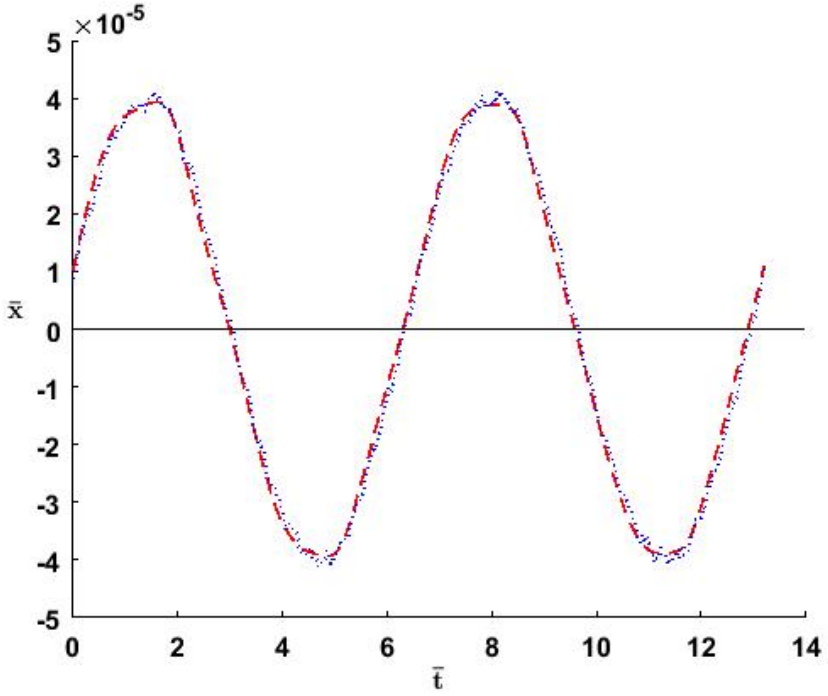

Figure 3.18: Position versus time of circuit 2 at 0.95/rev for two cycles. The simulation result is the red dashed line while the experimental result is the blue dotted line.

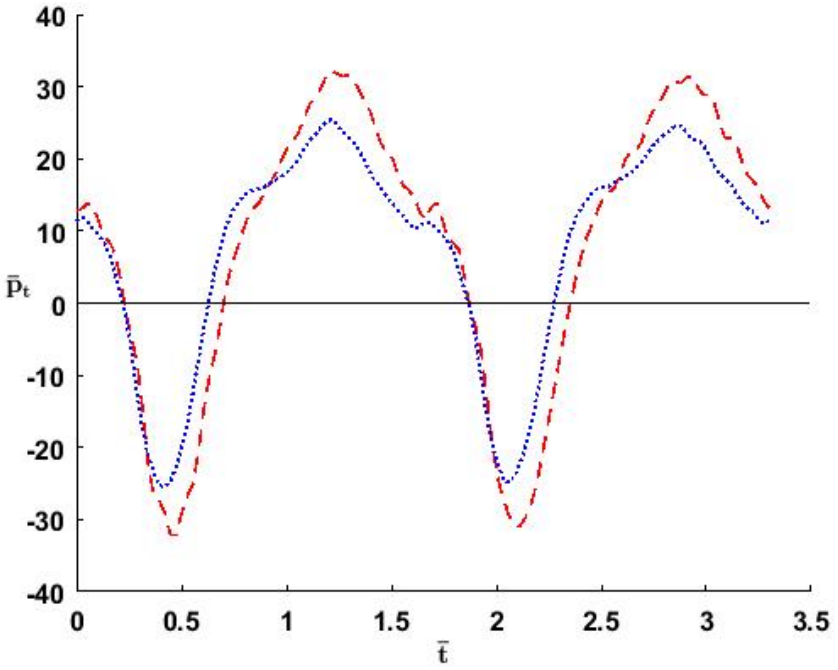

Figure 3.19: Pressure in the top chamber versus time of circuit 2 at 3.81/rev for two cycles. The simulation result is the red dashed line while the experimental result is the blue dotted line.

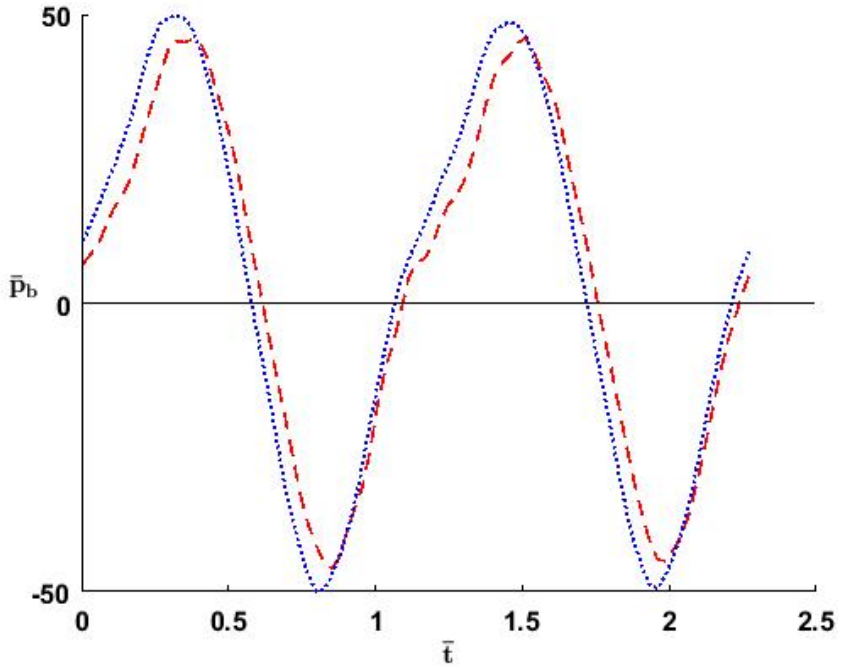

Figure 3.20: Pressure in the bottom chamber versus time of circuit 2 at 5.52/rev for two cycles. The simulation result is the red dashed line while the experimental result is the blue dotted line.

3.5.3 Circuit 3

The uncorrected fluid resistance, $\overline{R}_{fu}$, is 1.357×10^7 and the uncorrected inertance, $\overline{I}_u$, is 1.459×10^9. The frequency spectrum for the dynamic stiffness amplitude is illustrated in Figure 3.21. The longer fluid track will again cause both resistance and inertance to increase and thus the notch frequency further shifts left and contains a slightly shallower valley in comparison with the previous two circuits. The experimental notch frequency is approximately 4.1/rev while the simulation predicts that the notch frequency will occur at 3.78/rev. The error in the notch frequency seems to be trending up with the longer fluid tracks as it reaches 7.8% for circuit 3. The frequency spectrum for the amplitude of the pressure in the top chamber divided by force is illustrated in Figure 3.22. The amplitude is again predicted very well when accounting for the inaccuracy in the notch frequency.

Force versus position at 3.62/rev is illustrated in Figure 3.23. The simulation is able to accurately predict the shape of the curve, but it overpredicts the displacement amplitude. The bow tie shape occurs when the vertical axis frequency is double the frequency of the horizontal axis and the phase difference is a multiple of 90°. The amplitudes and phases for the first three harmonics of the input frequency are illustrated in Figure 3.24 and Figure 3.25 for the force input and displacement results, respectively. The force input has the largest amplitude at the second harmonic, but it also has signficant amplitudes at the first and third harmonics. The displacement results show a dominating peak in the amplitude at the input frequency. The phases at the second harmonic of the force input and the first harmonic of the displacement are both close to -90°. Thus Figure 3.23 has the bow tie shape due to the dominant force amplitude having double the frequency of the dominant displacement amplitude and zero phase shift. The amplitudes from the

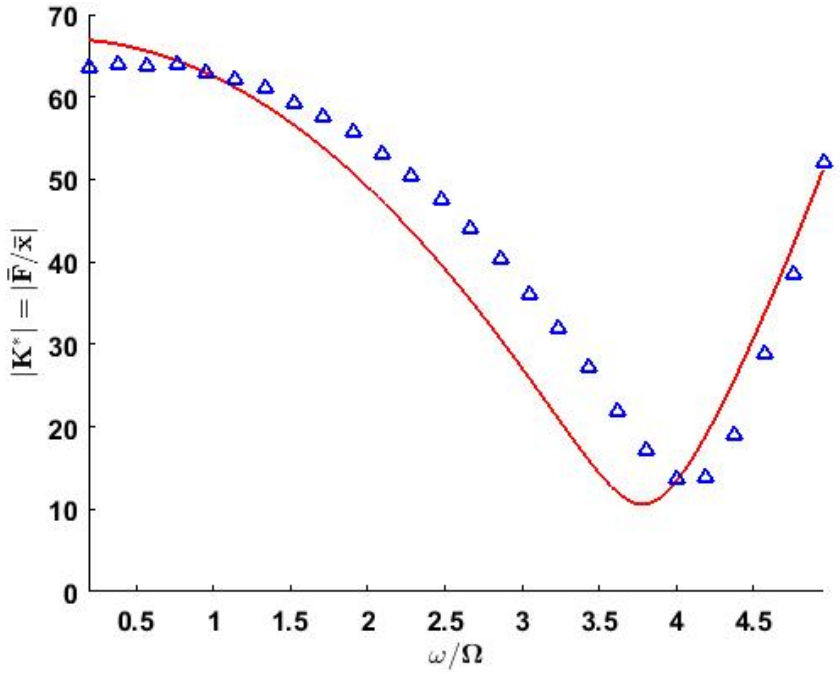

Figure 3.21: Dynamic stiffness amplitude of circuit 3. The simulation result is the red line while the experimental results are blue triangles.

other harmonics cause skewing of the bow tie.

The corresponding pressure in the top chamber versus force plot at 3.81/rev is illustrated in Figure 3.26. Similar to the force versus displacement curve, the simulation is able to accurately predict the shape of the curve, but it overpredicts the pressure amplitude. The amplitude and phase for the first three harmonics of the pressure are illustrated in Figure 3.27. There are large pressure amplitudes at the first two harmonics that are equal in size. The phase is close to 90° for the first harmonic and -90° for the second harmonic. A 45° degree line occurs when the frequencies between the horizontal and vertical axes are equal and the phases are separated by a multiple of 180°. Thus the pressure in the top chamber versus force plot is a combination of a 45° degree line due to amplitudes from the pressure and

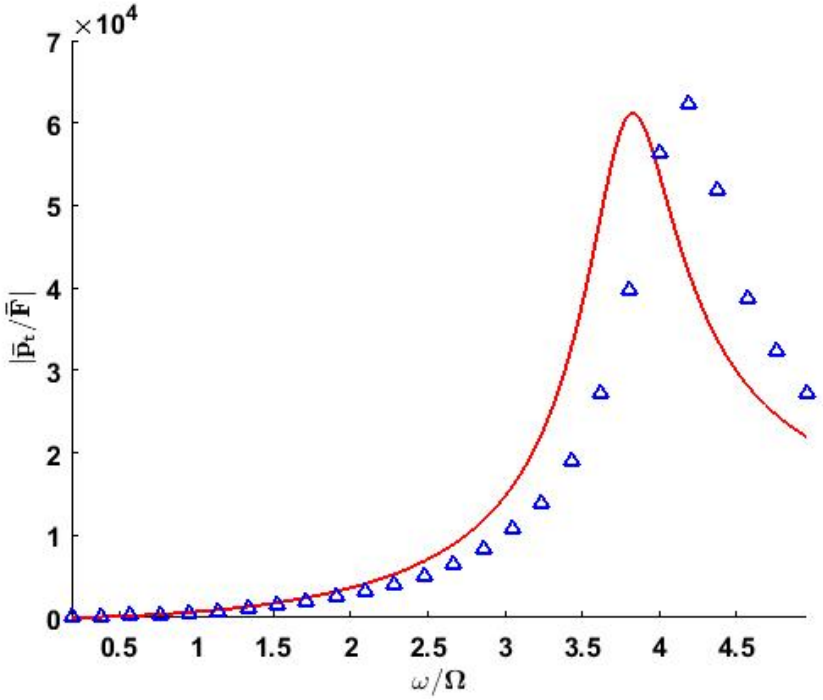

Figure 3.22: Amplitude of the pressure in the top chamber divided by force for circuit 3. The simulation result is the red line while the experimental results are blue triangles.

force at the second harmonic with zero phase shift and a vertical bow tie due to the pressure amplitude at the first harmonic and the force amplitude at the second harmonic with a 180° phase shift.

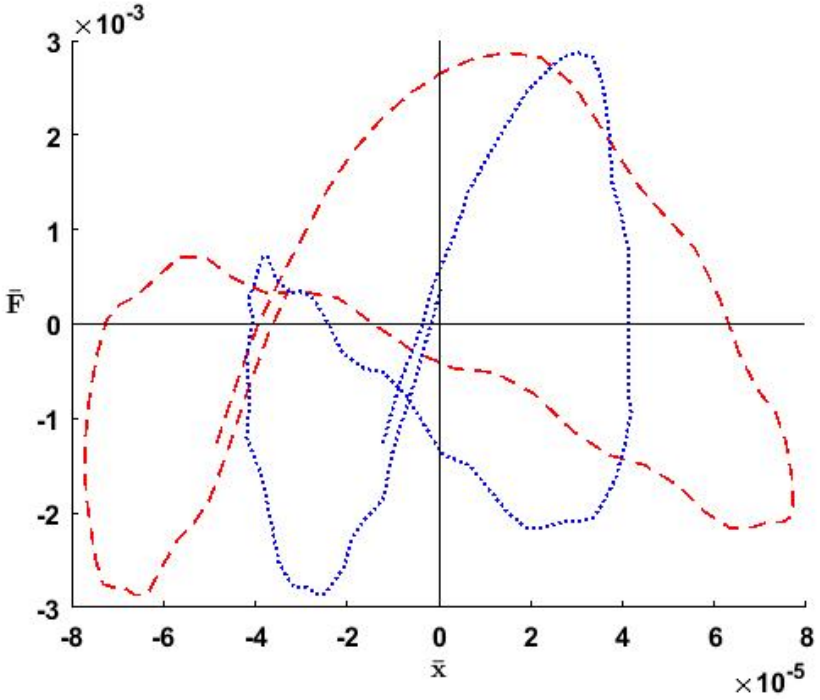

Figure 3.23: Force versus position of circuit 3 at 3.62/rev for one cycle. The simulation result is the red dashed line while the experimental result is the blue dotted line.

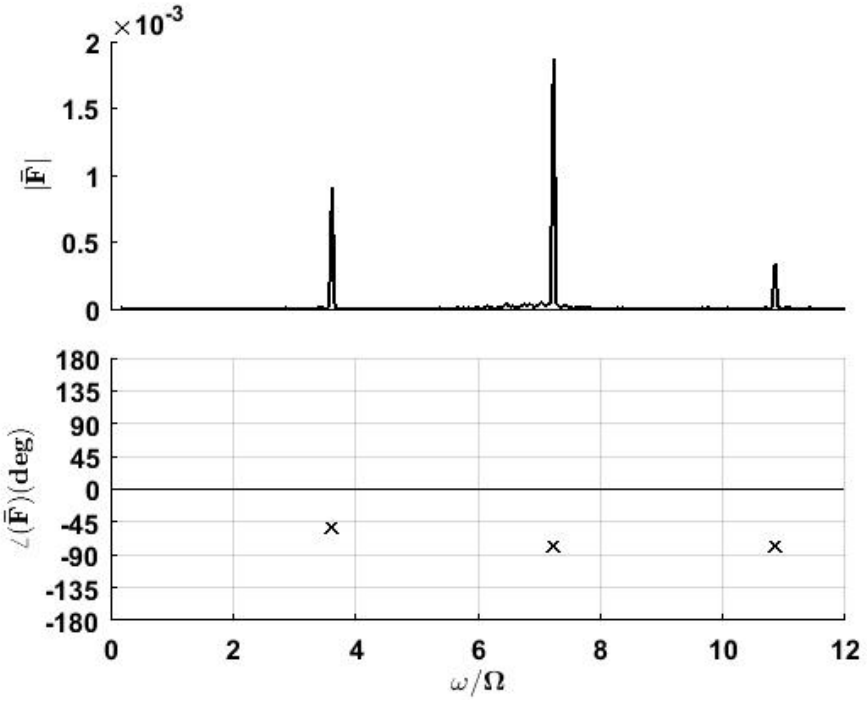

Figure 3.24: Force magnitude and phase of circuit 3 at 3.62/rev. The black color indicates that force is the input.

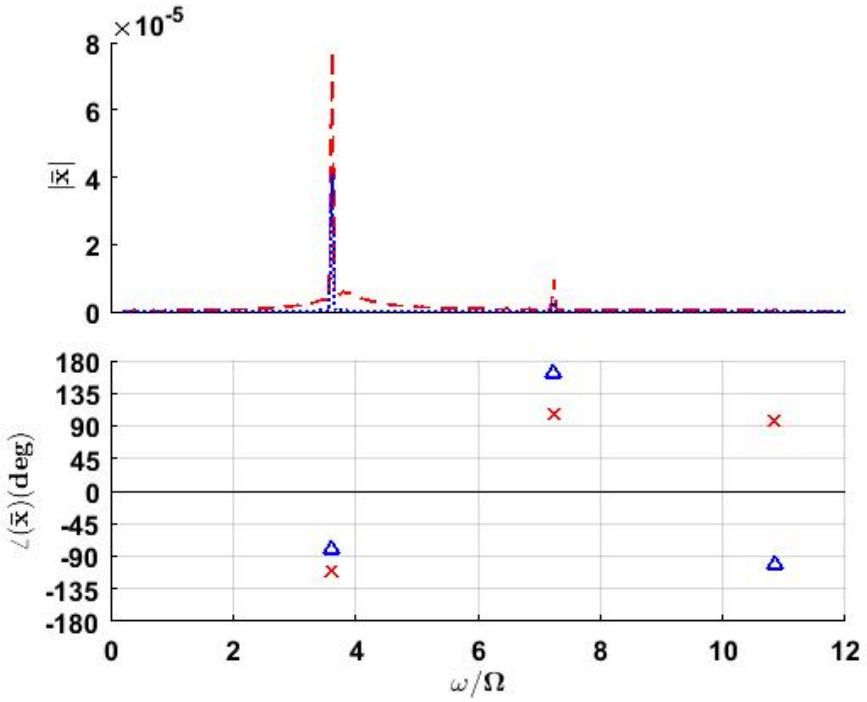

Figure 3.25: Position magnitude and phase of circuit 3 at 3.62/rev. The simulation result is the red dashed line in the magnitude plot and a red x in the phase plot while the experimental result is the blue dotted line in the magnitude plot and a blue triangle in the phase plot.

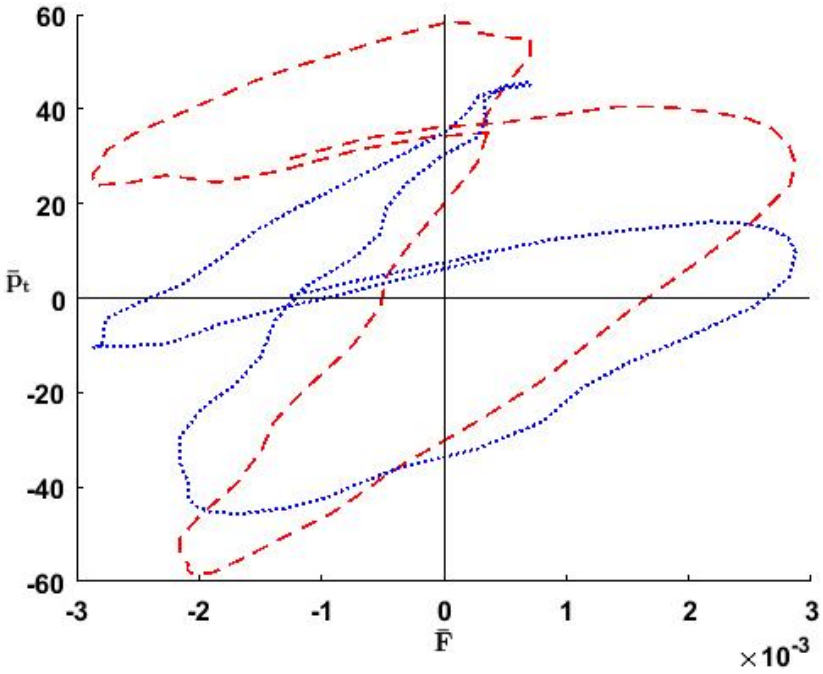

Figure 3.26: Pressure in the upper chamber versus force of circuit 3 at 3.62/rev for one cycle. The simulation result is the red dashed line while the experimental result is the blue dotted line.

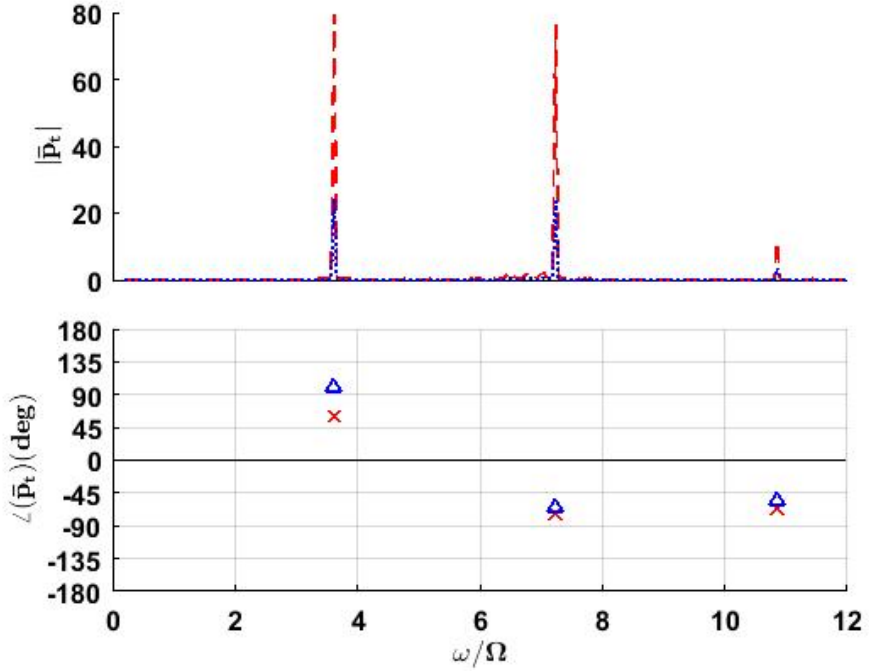

Figure 3.27: Pressure in the top chamber magnitude and phase for circuit 3 at 3.62/rev. The simulation result is the red dashed line in the magnitude plot and a red x in the phase plot while the experimental result is the blue dotted line in the magnitude plot and a blue triangle in the phase plot.

3.5.4 Circuit 4 Valve Closing Study

The dynamic stiffness amplitudes for multiple valves positions are illustrated in Figure 3.28. The model was unable to accurately predict the response when the FPL design parameters were input, so an empirical parameter study with constant coefficients was used to minimize the error in order to match the dynamic stiffness at each of the valve positions. The model predictions and experiment were set up with the expectation that the notch frequency for the fully open valve would be similar to the notch frequency from circuit 2 (∼4.8/rev). However, the figure shows that the notch frequency is actually approximately 3.8/rev. Using the method established in Section 3.4, the simulation is able to accurately match the experiment at each valve position. The values of each parameter that minimized the dynamic stiffness for each valve position are enumerated in Table 3.2.

Table 3.2: Fluidic Pitch Link Properties for Valve Closing Study

Property	Fully Open	3 Turns Closed	5 Turns Closed	7 Turns Closed	Fully Closed
$\overline{I}$	1.301×10^{9}	1.858×10^{9}	1.858×10^{9}	1.858×10^{9}	1.114×10^{9}
$\overline{R}_f$	1.349×10^{9}	2.575×10^{9}	1.839×10^{11}	7.970×10^{10}	1.594×10^{11}
$\overline{k}_d$	66.78	66.78	63.27	59.75	98.41
$\overline{A}$	3.945×10^{-5}	3.945×10^{-5}	6.136×10^{-5}	2.191×10^{-5}	2.191×10^{-5}
$\overline{c}_d$	8.048×10^{-2}	8.048×10^{-2}	8.048×10^{-2}	8.048×10^{-2}	8.048×10^{-2}
$\overline{C}_t$	1.483×10^{-12}	1.483×10^{-12}	1.032×10^{-8}	5.547×10^{-13}	5.547×10^{-13}
$\overline{C}_b$	1.483×10^{-12}	1.483×10^{-12}	1.032×10^{-8}	5.547×10^{-13}	5.547×10^{-13}
$\overline{m}_p$	5.814×10^{-3}	5.814×10^{-3}	5.814×10^{-3}	5.814×10^{-3}	5.814×10^{-3}
$\overline{k}_1$	4.088×10^{10}	4.088×10^{10}	5.872×10^{6}	1.093×10^{11}	1.093×10^{11}
$\overline{k}_2$	130.4	130.4	63.29	112.2	150.9
$\overline{k}_{12}$	1.613×10^{6}	1.613×10^{6}	360.3	2.394×10^{6}	2.394×10^{6}

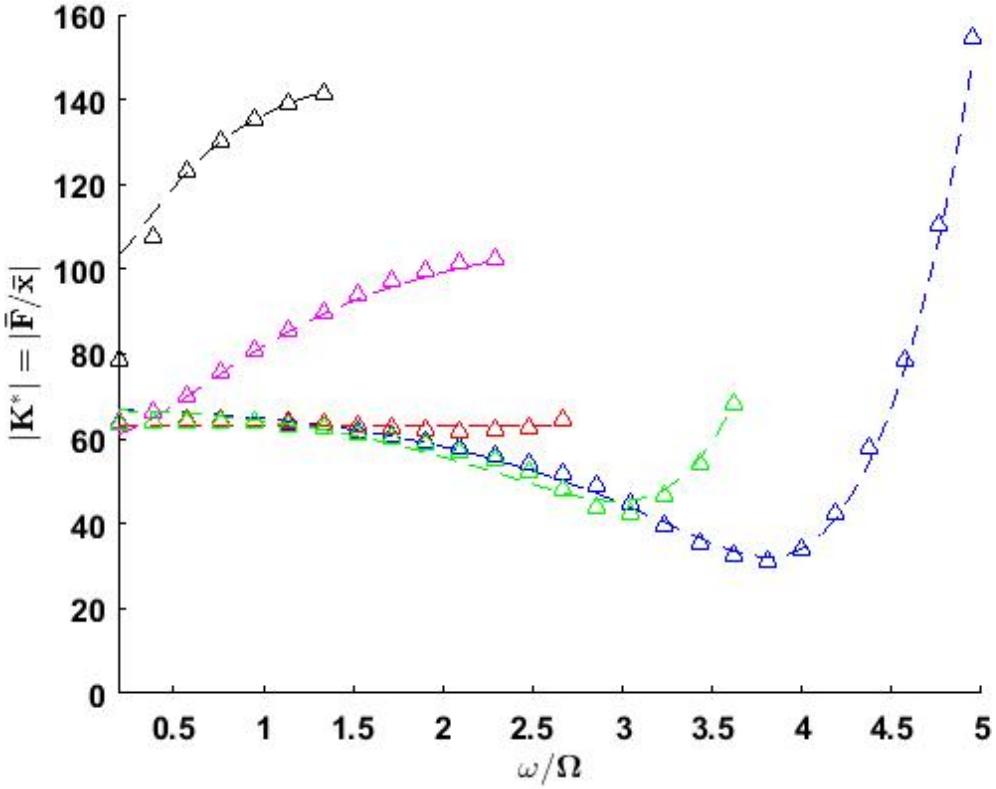

Figure 3.28: Dynamic stiffness amplitude for multiple valve positions. The simulation results are dashed lines while the experimental results are triangles. Blue is fully open, green is three turns closed, red is five turns closed, magenta is seven turns closed, and black is fully closed.

3.6 Conclusions

1. The fluidic pitch link model is able to accurately capture the shape and depth of the notch for the dynamic stiffness frequency response and for the peak in the pressure frequency responses for circuits 1-3.
2. The location accuracy of the notch frequency varies with increasing fluid track length. As fluid track length increased, so did the error. For circuit 1, the shortest track length, the error in the notch frequency was less than 2%

(.13/rev). For circuit 2, the medium track length, it was 3.5% (.17/rev). For circuit 3, the longest track length, it was 7.8% (0.32/rev). Local cavitation is a known issue that is unmodeled and may be a primary factor in altering the notch frequency from the predicted value to the experimental value.

3. The model predicted the notch frequency within 10% error for a notch frequency between 4.1/rev–6.8/rev thus satisfying our criteria for an accurate model.
4. The impact of the correction factors for the frequency dependent fluid resistance and inertia is significant and important when predicting fluidic pitch link performance.
5. There are unmodeled dynamics at low frequencies largely due to the frequency dependence of the elastomer.
6. The model does not accurately predict the dynamic stiffness amplitude of the fluidic pitch link when there is an extra flow restriction introduced into the fluid track as in the valve closing study performed using circuit 4. However, the model is capable of matching the dynamic stiffness when tuned empirically even when using constant coefficients for the fluidic pitch link parameters. Before empirically matching the test results, the original simulation predictions drastically overstated the notch frequency, even for the fully open case, which was expected to be similar to the results of circuit 2. The softening may be due to local cavitation or eddies that could be forming near the valve.
7. Though the simplicity of the model is one of its chief benefits, some of the error observed is likely attributed to this fact as well. To improve the understanding of the flow through the inertia track and near the needle valve and to model those features better, a computational fluid dynamics analysis

would be beneficial. This would drastically increase model complexity.

Chapter 4
Conclusions and Recommendations for Future Work

4.1 Pitch-Flap Stability of an Articulated Rotor with Fluidic Pitch Links

Fluidic pitch links are a passive vibration reduction device for helicopters. Previous studies explored hub vibration using a comprehensive aeroelastic similuation. However, prior to this investigation, stability impacts had not been explored. For the stability model, the rotor is articulated and is modeled by rigid pitch and rigid flap degrees of freedom. Quasi-steady aerodynamics are used for the lift and moment terms in the aeroelastic model. The control system stiffness is modeled as an axial spring. The fluidic pitch links have two degrees of freedom: axial displacement of the piston, which is directly related to pitch, and volume of fluid entering the inertia track. A positive impact on aeroelastic stability from several fluidic pitch

link designs are shown for hover. The positive stability margins found for the fluidic pitch links in hover are marginally affected by the periodic terms that appear in forward flight. The fluidic pitch links help stabilize the pitch mode and enable substantially larger aft center of gravity offsets to be used in rotor design.

The following conclusions were drawn from the analysis:

1. Fluidic pitch links can be used to add damping into the pitch mode thus enabling a higher CG offset for helicopters. While the baseline case goes unstable at 12% CG offset, there are fluidic pitch link designs that retain significant stability margins under these conditions. These fluidic pitch link designs could open up the blade design space by enabling decreased leading edge weight or a redistribution of mass in blade designs that may have previously resulted in an unstable system.
2. Increasing fluidic resistance enables damping to be added into the pitch mode. Fluidic pitch link designs can show more than 10% damping added into the pitch mode. This can enable a higher CG offset for helicopter rotor blades or stabilize unstable ones.
3. Reducing capacitance for a rotor configuration with a CG offset can increase the stability margin until fluid capacitance becomes too low causing the rigid pitch link case to be recovered.
4. The positive stability margins that are found for the fluidic pitch links in hover are marginally affected by the periodic terms that appear in forward flight and the margins are better across the entire range of advance ratios.
5. Fluidic pitch links show great potential for improving hover stability or enabling blade design changes without causing an unstable condition in forward flight.

4.2 Experimental Validation of a Fluidic Pitch Link Model

The model for a double pumper fluidic pitch link was derived. This is a more viable and popular choice than the single pumper model due to greater safety and reduced risk of cavitation. In this investigation, a prototype fluidic pitch link was designed, built, and tested at LORD Corporation. Displacement, load, and pressure were recorded during testing. Frequency and time response results were compared between simulation and experiment to validate the model. Development of a swappable inertia track and use of a needle valve enabled systematic variation of the inertance and resistance properties. Varying inertance and resistance properties enabled validation of the model for several notch frequency locations as well as varying magnitudes. Pressure taps were also added to the top and bottom fluid chambers to record pressure.

The model was tested in four different configurations. Three different track lengths provided three different inertance values. A fourth configuration involved testing of a split track with a needle valve and compression fittings. Resistance was varied in this configuration by closing down the needle valve.

Two analysis methods were used for successful validation of the fluidic pitch link model. The first method applied fluidic pitch link design parameters to a simulation for comparison of our model with recorded experimental data in the time-domain and frequency-domain. This method was employed to simulate circuits 1-3 and was used to evaluate the validity of the model to predict the experimental results. The second method utilized an empirical parameter study to match the time-domain and frequency-domain data from testing via simulation results. This method was

employed for the valve closing study using circuit 4. The objective of this method was to evaluate the validity of the model to match the experimental results if the first method failed and to make note of any missing dynamics.

The following conclusions were drawn from the analysis:

1. The fluidic pitch link model is able to accurately capture the shape and depth of the notch for the dynamic stiffness frequency response and for the peak in the pressure frequency responses for circuits 1-3.
2. The location accuracy of the notch frequency varies with increasing fluid track length. As fluid track length increased, so did the error. For circuit 1, the shortest track length, the error in the notch frequency was less than 2% (.13/rev). For circuit 2, the medium track length, it was 3.5% (.17/rev). For circuit 3, the longest track length, it was 7.8% (0.32/rev). Local cavitation is a known issue that is unmodeled and may be a primary factor in altering the notch frequency from the predicted value to the experimental value.
3. The model predicted the notch frequency within 10% error for a notch frequency between 4.1/rev–6.8/rev thus satisfying our criteria for an accurate model.
4. The impact of the correction factors for the frequency dependent fluid resistance and inertia is significant and important when predicting fluidic pitch link performance.
5. There are unmodeled dynamics at low frequencies largely due to the frequency dependence of the elastomer.
6. The model does not accurately predict the dynamic stiffness amplitude of the fluidic pitch link when there is an extra flow restriction introduced into the fluid track as in the valve closing study performed using circuit 4. However, the model is capable of matching the dynamic stiffness when

tuned empirically even when using constant coefficients for the fluidic pitch link parameters. Before empirically matching the test results, the original simulation predictions drastically overstated the notch frequency, even for the fully open case, which was expected to be similar to the results of circuit 2. The softening may be due to local cavitation or eddies that could be forming near the valve.

7. Though the simplicity of the model is one of its chief benefits, some of the error observed is likely attributed to this fact as well. To improve the understanding of the flow through the inertia track and near the needle valve and to model those features better, a computational fluid dynamics analysis would be beneficial. This would drastically increase model complexity.

4.3 Recommended Future Work

The fluidic pitch link model is reasonably accurate at this stage, but several tasks can be completed to improve the accuracy at low frequency, the location of the notch frequency, and gain a better overall understanding of the fluid dynamics through the inertia track. To improve the accuracy at low frequencies, a finite element model can be used to more accurately model the behavior of the elastomer. Brackbill et al. [106], [107] and Marr et al. [108] have explored using the method of anelastic displacement fields to model the elastomer in order to capture temperature and frequency dependencies. This method could be used to improve the elastomer modeling. However, it is to be noted that this method increases model size and complexity very quickly. Alternatively, the frequency and temperature dependences of the elastomer could be empirically added into the model by use of a frequency dependent correction factor for the elastomer stiffness, k_d, and elastomer damping,

c_d. Additionally, a computational fluid dynamics (CFD) model of the flow through the inertia track would enhance the understanding of the fluid motion; specifically, exploration of local cavitation and the flow regime near the needle valve would be beneficial. The results of this study could be used to develop a semi-empirical, CFD augmented analytical model as was performed by Marr et al. in [109] to explore damper behavior.

In addition to enhancing the model, it would be beneficial to perform a hub loads reduction study combined with a stability analysis. Emphasizing practical fluidic pitch link parameters for a given helicopter configuration during this study would also be impactful. This could also be combined with studies focused on increasing aircraft performance and forward flight maneuverability, reducing weight, or decreasing the noise envelop while maintaining stability. One final point of interest is determination of the centrifugal force effects on a fluidic pitch link that is moving in curvilinear motion. It remains to be studied whether the stress concentration at the rod end to fluidic pitch link body connections is high enough to pose the risk of fracture at either of those locations in the normal direction, inward toward the center of curvature.

Appendix A
Equations for Pitch-Flap Stability Model

A.1 Unsteady Aerodynamics Moments, Force, and Air Velocity Terms

A.1.1 Pitch and Flap Aerodynamic Moments

$$\overline{M}_\beta = \gamma \int_0^1 \frac{xL}{\Omega^2 \rho a c R^2} dx \tag{A.1}$$

$$\overline{M}_\theta = \gamma \int_0^1 \frac{M_a}{\Omega^2 \rho a c R^3} dx \tag{A.2}$$

A.1.2 Section Aerodynamic Lift Force and Moment

$$L = \frac{1}{2}\rho a c \left[\left(u_T^2 + \frac{1}{4} c \dot{u}_T \right) \theta + \frac{1}{2} c u_T \dot{\theta} + \frac{1}{2} c \left(\Omega u_T - \frac{1}{2} \dot{u}_R \right) \beta + \frac{1}{4} c \left(\frac{1}{4} c \Omega - u_R \right) \dot{\beta} - u_P u_T \right] \tag{A.3}$$

$$M_a = -\frac{1}{32}\rho a c^3 \left[\dot{u}_T \theta + u_T \dot{\theta} + \left(\Omega u_T - \dot{u}_R \right) \beta + \left(u_R - \frac{3}{8} c \Omega \right) \dot{\beta} \right] \tag{A.4}$$

A.1.3 Tangential, Radial, and Perpendicular Section Air Velocities

$$u_T = \Omega r + \Omega R \mu \sin\psi \tag{A.5}$$

$$u_R = \Omega R \mu \cos\psi \tag{A.6}$$

$$u_P = \lambda \Omega R + r\dot{\beta} + u_R \beta \tag{A.7}$$

A.2 Generalized Mass Matrix Elements

$$M_{1,1} = 1 \tag{A.8}$$

$$M_{1,2} = M_{2,1} = -\frac{3}{2}\frac{x_I}{c}\frac{c}{R} \tag{A.9}$$

$$M_{1,3} = M_{1,4} = M_{2,3} = M_{2,4} = M_{3,1} = M_{3,2} = M_{3,4} = M_{4,1} = M_{4,2} = M_{4,3} = 0 \tag{A.10}$$

$$M_{2,2} = I_f^* + \frac{m_p l_{ph}^2}{I_b} \tag{A.11}$$

$$M_{3,3} = \frac{m_c l_{ph} R}{I_b} \tag{A.12}$$

$$M_{4,4} = \frac{3IR^3}{m_b} \tag{A.13}$$

A.3 Generalized Damping Matrix Elements

$$C_{1,1} = -\gamma \left(\frac{1}{64} \left(\frac{c}{R} \right)^2 - C' \left(\frac{1}{8} + \frac{1}{6}\mu \sin\psi \right) \right.$$

$$-\frac{1}{8}\frac{c}{R}\mu\cos\psi\Big) \tag{A.14}$$

$$C_{1,2} = -\gamma\frac{1}{4}\frac{c}{R}\left(1 + 2C'\left(\frac{1}{6} + \frac{1}{4}\mu\sin\psi\right)\right) \tag{A.15}$$

$$C_{1,3} = C_{1,4} = C_{2,4} = C_{3,1} = C_{3,4} =$$
$$C_{4,1} = C_{4,2} = C_{4,3} = 0 \tag{A.16}$$

$$C_{2,1} = -\gamma\left(\left(\frac{c}{R}\right)^2\mu\cos\psi - \frac{3}{256}\left(\frac{c}{R}\right)^3\right) \tag{A.17}$$

$$C_{2,2} = \gamma\frac{1}{16}\left(\frac{c}{R}\right)^2\left(\frac{1}{2} + \mu\sin\psi\right) + \frac{c_d l_{ph}^2}{I_b\Omega} \tag{A.18}$$

$$C_{2,3} = -C_{3,3} = \frac{-c_d l_{ph} R}{I_b\Omega} \tag{A.19}$$

$$C_{3,2} = \frac{-c_d l_{ph}^2}{I_b\Omega} \tag{A.20}$$

$$C_{4,4} = \frac{3R_f R^3}{m_b\Omega} \tag{A.21}$$

A.4 Generalized Stiffness Matrix Elements

$$K_{1,1} = 1 + \frac{K_\beta}{I_b\Omega^2} - \gamma\Big(C'\left(\frac{1}{6} + \frac{1}{4}\mu\sin\psi\right)\left(\frac{1}{2}\frac{c}{R} - \mu\cos\psi\right) + \frac{1}{16}\frac{c}{R}\mu\sin\psi\Big) \tag{A.22}$$

$$K_{1,2} = -\frac{3}{2}\frac{x_I}{c}\frac{c}{R} - \gamma\Big(C'\left(\frac{1}{8} + \frac{1}{3}\mu\sin\psi + \frac{1}{4}\mu^2\sin psi^2\right) + \left(\frac{1}{16}\frac{c}{R}\mu\cos\psi\right)\Big) \tag{A.23}$$

$$K_{1,3} = K_{1,4} = K_{1,3} = K_{3,1} = K_{4,1} = 0 \tag{A.24}$$

$$K_{2,1} = -\frac{3}{2}\frac{x_I}{c}\frac{c}{R} - \gamma\frac{1}{64}\left(1 + 4\mu\sin\psi\right) \tag{A.25}$$

$$K_{2,2} = I_f^* + \gamma\frac{1}{32}\left(\frac{c}{R}\right)^2\mu\cos\psi + \frac{\left(k_d + \frac{A^2}{C_p}\right)l_{ph}^2}{I_b\Omega^2} \tag{A.26}$$

$$K_{2,3} = \frac{-\left(k_d + \frac{A^2}{C_p}\right)l_{ph}R}{I_b\Omega^2} \tag{A.27}$$

$$K_{2,4} = -K_{3,4} = K_{4,2} = \frac{-3Al_{ph}}{C_p m_b\Omega^2} \tag{A.28}$$

$$K_{3,2} = \frac{-\left(k_d + \frac{A^2}{C_p}\right)l_{ph}^2}{I_b\Omega^2} \tag{A.29}$$

$$K_{3,3} = \frac{\left(k_d + \frac{A^2}{C_p} + K_{cs}\right)l_{ph}R}{I_b\Omega^2} \tag{A.30}$$

$$K_{4,3} = \frac{3AR}{C_p m_b\Omega^2} \tag{A.31}$$

$$K_{4,4} = \frac{3\left(\frac{1}{C_a} + \frac{1}{C_p}\right)}{m_b\Omega^2} \tag{A.32}$$

A.5 Spring Element Pitch Link Stiffness

$$K_\theta = l_{ph}\frac{K_{cs}K_{pl}}{K_{cs} + K_{pl}} \tag{A.33}$$

A.6 First-Order Form

$$[A] = \begin{bmatrix} \underline{0} & \underline{I} \\ -\underline{M}^{-1}\underline{K} & -\underline{M}^{-1}\underline{C} \end{bmatrix} \tag{A.34}$$

Table A.1: Feathering Inertia Values by CG Offset

$\frac{x_I}{c}(\%)$	I_f^* $(\times 10^{-4})$
0	10
1	9.63
2	9.27
3	8.93
4	8.60
5	8.31
6	8.02
7	7.76
8	7.54
9	7.33
10	7.13
11	6.97
12	6.82

Appendix B
Non-dimensionalization Equations for Fluidic Pitch Link Testing

$$\overline{I} = \frac{IR^3}{m_b} \tag{B.1}$$

$$\overline{m}_p = \frac{m_p}{m_b R} \tag{B.2}$$

$$\overline{R}_f = \frac{R^3 R_f}{m_b \Omega} \tag{B.3}$$

$$\overline{c}_d = \frac{c_d}{m_b \Omega R} \tag{B.4}$$

$$\overline{k}_1 = \frac{R^3 \left(\frac{1}{C_t} + \frac{1}{C_b}\right)}{m_b \Omega^2} \tag{B.5}$$

$$\overline{k}_{12} = \frac{AR \left(\frac{1}{C_t} + \frac{1}{C_b}\right)}{m_b \Omega^2} \tag{B.6}$$

$$\overline{k}_2 = \frac{A^2 \left(\frac{1}{C_t} + \frac{1}{C_b}\right) + k_d}{m_b \Omega^2 R} \tag{B.7}$$

$$\overline{F} = \frac{F}{m_b \Omega^2 R^2} \tag{B.8}$$

$$\overline{k}_d = \frac{k_d}{m_b \Omega^2 R} \tag{B.9}$$

$$\overline{C}_t = \frac{C_t m_b \Omega^2}{R^3} \tag{B.10}$$

$$\overline{C}_b = \frac{C_b m_b \Omega^2}{R^3} \tag{B.11}$$

$$\overline{A} = \frac{A}{R^2} \tag{B.12}$$

Bibliography

[1] ©Burkhard Domke (1988), "Main Rotor Head and Swashplate Assembly." [Online; accessed June 28, 2017].
URL http://www.b-domke.de/AviationImages/Rotorhead/0416.html

[2] Bir, G. (2008) "Multiblade Coordinate Transformation and Its Application to Wind Turbine Analysis," in *ASME Wind Energy Symposium*.

[3] Davis, M. W. and W. H. Weller (1988) "Application of Design Optimization Techniques to Rotor Dynamics Problems," *Journal of the American Helicopter Society*, **33**(3), pp. 42–50.

[4] Luca, S.-G., F. Chira, and V. Rosca (2005) "Passive, Active and Semi-Active Control Systems in Civil Engineering," *Constructil Arhitectura*, **3**, p. 4.

[5] Seeler, K. A. (2014) *System Dynamics: An Introduction for Mechanical Engineers*, Springer.

[6] Preumont, A. (2011) *Vibration Control of Active Structures: An Introduction*, vol. 179, Springer Science & Business Media.

[7] Johnson, C. D. (1995) "Design of Passive Damping Systems," *Journal of Vibration and Acoustics*, **117**(B), pp. 171–176.

[8] De Silva, C. W. (2005) *Vibration and Shock Handbook*, CRC Press.

[9] Smith, M. R. and W. S. Redinger (1999) "The Model 427 Pylon Isolation System," in *Annual Forum Proceedings – American Helicopter Society*, vol. 1, pp. 195–201.

[10] Wachs, M. A. (1973) *The Main Rotor Bifilar Absorber and Its Effect on Helicopter Reliability/Maintainability, Tech. rep.*, SAE Technical Paper.

[11] Igusa, T. and K. Xu (1994) "Vibration Control Using Multiple Tuned Mass Dampers," *Journal of Sound and Vibration*, **175**(4), pp. 491–503.

[12] Rana, R. and T. Soong (1998) "Parametric Study and Simplified Design of Tuned Mass Dampers," *Engineering Structures*, **20**(3), pp. 193–204.

[13] Ormondroyd, J. (1928) "Theory of the Dynamic Vibration Absorber," *Transaction of the ASME*, **50**, pp. 9–22.

[14] Paul, W. F. (1969) "Development and Evaluation of the Main Rotor Bifilar Absorber," in *Proceedings of the 25th American Helicopter Society Forum*.

[15] Miura, K., C. D. Rahn, and E. C. Smith (2014) "Passive Tailboom Vibration Control Using Fluidic Flexible Matrix Composite (F2MC) Tubes," in *Proceedings of the 55th AIAA/AS-ME/ASCE/AHS/ASC Structures, Structural Dynamics, and Materials Conference*.

[16] Krott, M., K. Miura, C. Rahn, and E. C. Smith (2016) "Finite Element Modeling of Fluidic Flexible Matrix Composite (F2MC) Treatments for Bending and Torsional Vibration Control," in *57th AIAA/ASCE/AHS/ASC Structures, Structural Dynamics, and Materials Conference*, p. 1479.

[17] Ogata, K. (1998) *System Dynamics*, vol. 3, Prentice Hall New Jersey.

[18] Flannelly, W. (1966) "The Dynamic Antiresonant Vibration Isolator," in *American Helicopter Society, 22nd Annual National Forum, Washington, D.C.*, pp. 152–160.

[19] Halwes, D. (1980) "LIVEâĂŤLiquid Inertia Vibration Eliminator," in *American Helicopter Society 36th Annual Forum, Washington, DC, May*, pp. 13–14.

[20] McGuire, D. P. (1994) "Fluidlastic Dampers and Isolators for Vibration Control in Helicopters," in *Proceedings of the 50th American Helicopter Society Annual Forum*.

[21] McGuire, D. P. (2003) "High Stiffness ("Rigid") Helicopter Pylon Vibration Isolation Systems," in *Annual Forum Proceedings–American Helicopter Society*, vol. 59, pp. 649–658.

[22] Anusonti-Inthra, P., F. Gandhi, and L. Miller (2003) "Reduction of Helicopter Vibration Through Cyclic Control of Variable Orifice Dampers," *Aeronautical Journal*, **107**(1077), pp. 657–672.

[23] Titurus, B. and N. Lieven (2009) "Modeling and Analysis of Semi-Active Dampers in Periodic Working Environments," *AIAA Journal*, **47**(10), pp. 2404–2416.

[24] Titurus, B. and N. Lieven (2010) "Integration of Hydraulic Lag-Damper Models with Helicopter Rotor Simulations," *Journal of Guidance, Control, and Dynamics*, **33**(1), pp. 200–211.

[25] Titurus, B., J. D. Bois, and N. Lieven (2012) "Modeling and Testing of a Semiactive Hydraulic Damper in Periodic Working Regimes," *AIAA journal*, **50**(4), pp. 844–854.

[26] Titurus, B. (2013) "Vibration Control in a Helicopter with Semi-Active Hydraulic Lag Dampers," *Journal of Guidance, Control, and Dynamics*, **36**(2), pp. 577–588.

[27] Hiemenz, G. J., Y.-T. Choi, and N. M. Wereley (2007) "Semi-Active Control of Vertical Stroking Helicopter Crew Seat for Enhanced Crashworthiness," *Journal of Aircraft*, **44**(3), pp. 1031–1034.

[28] Lotfi-Gaskarimahalle, A., Y. Shan, S. Li, C. D. Rahn, C. E. Bakis, and K. Wang (2008) "Stiffness Shaping for Zero Vibration Fluidic Flexible Matrix Composites," in *ASME 2008 Conference on Smart Materials, Adaptive Structures and Intelligent Systems*, American Society of Mechanical Engineers, pp. 409–417.

[29] Philen, M. (2011) "Fluidic Flexible Matrix Composite Semi-Active Vibration Isolation Mounts," *Journal of Intelligent Material Systems and Structures*.

[30] Clark, W. W. (1999) "Semi-Active Vibration Control with Piezoelectric Materials as Variable-Stiffness Actuators," in *1999 Symposium on Smart Structures and Materials*, International Society for Optics and Photonics, pp. 123–130.

[31] Heverly II, D. E. (2002) *Optimal Actuator Placement and Active Structure Design for Control of Helicopter Airframe Vibrations*, Ph.D. thesis, The Pennsylvania State University.

[32] von Hardenberg, P. (1984) "Helicopter Airframe Variable Tune Vibration Absorber," in *AIAA, AHS, ASEE, Aircraft Design Systems and Operations Meeting, San Diego, CA*, vol. 31.

[33] Staple, A. E. (1989) "An Evaluation of Active Control of Structural Response as a Means of Reducing Helicopter Vibration," in *Proceedings of the 15th European Rotorcraft Forum*, pp. 51–67.

[34] Welsh, W. A., P. C. Von Hardenberg, P. W. Von Hardenberg, and A. E. Staple (1990) "Test and Evaluation of Fuselage Vibration Utilizing Active Control of Structural Response (ACSR) Optimized to ADS-27," in *AHS, Annual Forum, 46 th, Washington, DC, Proceedings.*, vol. 1, pp. 21–37.

[35] Chiu, T. and P. P. Friedmann (1997) "An Analytical Model for ACSR Approach to Vibration Reduction in a Helicopter Rotor-Flexible Fuselage System," *Aeronautical Journal*, **101**(1009), pp. 399–408.

[36] Shaw Jr, J. (1968) *Higher Harmonic Blade Pitch Control for Helicopter Vibration Reduction: A Feasibility Study*, *Tech. rep.*, DTIC Document.

[37] Robinson, L. H. and P. P. Friedmann (1991) "A Study of Fundamental Issues in Higher Harmonic Control Using Aeroelastic Simulation," *Journal of the American Helicopter Society*, **36**(2), pp. 32–43.

[38] Nguyen, K. and I. Chopra (1990) "Application of Higher Harmonic Control to Rotors Operating at High Speed and Thrust," *Journal of the American Helicopter Society*, **35**(3), pp. 78–89.

[39] McHugh, F. J. and J. Shaw (1978) "Helicopter Vibration Reduction with Higher Harmonic Blade Pitch," *Journal of the American Helicopter Society*, **23**(4), pp. 26–35.

[40] Walsh, D. M. (1986) *Flight Tests of an Open Loop Higher Harmonic Control System on an S-76A Helicopter*, Master's thesis, Florida Atlantic University.

[41] Wood, E. R., R. W. Powers, J. H. Cline, and C. E. Hammond (1985) "On Developing and Flight Testing a Higher Harmonic Control System," *Journal of the American Helicopter Society*, **30**(1), pp. 3–20.

[42] Friedmann, P. P. and T. A. Millott (1995) "Vibration Reduction in Rotorcraft Using Active Control: A Comparison of Various Approaches," *Journal of Guidance, Control, and Dynamics*, **18**(4), pp. 664–673.

[43] Ham, N. (1980) "A Simple System for Helicopter Individual-Blade-Control and Its Application to Gust Alleviation," .

[44] Ham, N. D. (1984) "Helicopter individual-blade-control and its applications," .

[45] Guinn, K. F. (1982) "Individual Blade Control Independent of a Swashplate," *Journal of the American Helicopter Society*, **27**(3), pp. 25–31.

[46] Jacklin, S. A., J. A. Leyland, and A. Blaas (1993) "Full-Scale Wind Tunnel Investigation of a Helicopter Individual Blade Control System," *AIAA paper*, (93-1361), pp. 576–586.

[47] Jacklin, S. A., A. Blaas, D. Teves, R. Kube, and W. Warmbrodt (1994) "Reduction of Helicopter BVI Noise, Vibration, and Power Consumption Through Individual Blade Control," .

[48] Richter, P. and H.-D. EISBRECHER (1990) "Design and First Tests of Individual Blade Control Actuators," .

[49] Millott, T. A. and P. P. Friedmann (1994) "Vibration Reduction in Helicopter Rotors Using an Actively Controlled Partial Span Trailing Edge Flap Located on the Blade," .

[50] Zhang, J., E. C. Smith, and K. Wang (2004) "Active-Passive Hybrid Optimization of Rotor Blades with Trailing Edge Flaps," *Journal of the American Helicopter Society*, **49**(1), pp. 54–65.

[51] Léon, O. and F. Gandhi (2009) "Rotor Power Reduction Using Multiple Spanwise-Segmented, Optimally-Actuated Trailing-Edge Flaps," .

[52] Andrews, J., W. Welsh, R. Altieri, and J. DiOttavio (2014) "Ground and Flight Testing of a Hub Mounted Vibration Suppression System," in *AHS 70th Annual Forum, Montreal, Quebec, Canada*.

[53] Miller, R. H. and C. W. Ellis (1956) "Helicopter Blade Vibration and Flutter," *Journal of the American Helicopter Society*, **1**(3), pp. 19–38.

[54] Chou, P. C. (1958) "Pitch-Lag Instability of Helicopter Rotors," *Journal of the American Helicopter Society*, **3**(3), pp. 30–39.

[55] Friedmann, P. P. and D. H. Hodges (2003) "Rotary Wing Aeroelasticity – A Historical Perspective," *Journal of Aircraft*, **40**(6), pp. 1019–1046.

[56] Loewy, R. G. (1957) "A Two-Dimensional Approximation to the Unsteady Aerodynamics of Rotary Wings," *Journal of the Aeronautical Sciences*, **24**(2).

[57] Theodorsen, T. (1949) "General Theory of Aerodynamic Instability and the Mechanism of Flutter," .

[58] Greenberg, J. M. (1947) *Airfoil in Sinusoidal Motion in a Pulsating Stream, Tech. Rep. NACA-TN-1326*, NACA.

[59] Edwards, J. W. (1979) "Unsteady Aerodynamic Modeling for Arbitrary Motions," *AIAA Journal*, **17**(4), pp. 365–374.

[60] Dinyavari, M. and P. Friedmann (1986) "Application of Time-Domain Unsteady Aerodynamics to Rotary-Wing Aeroelasticity," *AIAA journal*, **24**(9), pp. 1424–1432.

[61] Dinyavari, M. and P. Friedmann (1989) "Time Domain Unsteady Incompressible Cascade Airfoil Theory for Helicopter Rotors in Hover," *AIAA Journal*, **27**(3), pp. 257–267.

[62] Young, M. I. (1964) "A Theory of Rotor Blade Motion Stability in Powered Flight," *Journal of the American Helicopter Society*, **9**(3), pp. 12–25.

[63] Hohenemser, K. H. and P. W. Heaton (1967) "Aeroelastic Instability of Torsionally Rigid Helicopter Blades," *Journal of the American Helicopter Society*, **12**(2), pp. 1–13.

[64] Houbolt, J. C. and G. W. Brooks (1958) *Differential Equations of Motion for Combined Flapwise Bending, Chordwise Bending, and Torsion of Twisted Nonuniform Rotor Blades*, *Tech. Rep. NACA-TR-1346*, NACA.

[65] Ormiston, R. A. and D. H. Hodges (1972) "Linear Flap-Lag Dynamics of Hingeless Helicopter Rotor Blades in Hover," *Journal of the American Helicopter Society*, **17**(2), pp. 2–14.

[66] Friedmann, P. and P. Tong (1973) "Non-Linear Flap-Lag Dynamics of Hingeless Helicopter Blades in Hover and in Forward Flight," *Journal of Sound and Vibration*, **30**(1), pp. 9–31.

[67] Ormiston, R. and W. Bousman (1975) "A Study of Stall-Induced Flap-Lag Instability of Hingeless Rotors," *Journal of the American Helicopter Society*, **20**(1), pp. 20–30.

[68] Friedmann, P. and J. Shamie (1977) "Aeroelastic Stability of Trimmed Helicopter Blades in Forward Flight," *Vertica*, **1**(3), pp. 189–211.

[69] Friedmann, P. (1977) "Influence of Modeling and Blade Parameters on the Aeroelastic Stability of a Cantilevered Rotor," *AIAA Journal*, **15**(2), pp. 149–158.

[70] Huber, H. (1973) "Effect of Torsion-Flap-Lag Coupling on Hingeless Rotor Stability," in *American Helicopter Society, Annual National Forum, 29 th, Washington, D. C.*

[71] Hansford, R. and I. Simons (1973) "Torsion-Flap-Lag Coupling on Helicopter Rotor Blades," *Journal of the American Helicopter Society*, **18**(4), pp. 2–12.

[72] Shamie, J. and P. Friedmann (1977) "Effect of Moderate Deflections on the Aeroelastic Stability of a Rotor Blade in Forward Flight," in *Procedings of 3rd European Rotorcraft and Powered Lift Aircraft Forum*, pp. 24–1.

[73] Friedmann, P. and S. Kottapalli (1982) "Coupled Flap-Lag-Torsional Dynamics of Hingeless Rotor Blades in Forward Flight," *Journal of the American Helicopter Society*, **27**(4), pp. 28–36.

[74] Anderson, W. (1976) *Rexor Rotorcraft Simulation Model*, [Department of Defense, Department of the Army, Army Materiel Development and Readiness Command, Army Aviation Research and Development Command], Army Air Mobility Research and Development Laboratory, Eustis Directorate.

[75] Johnson, W. (1981) "Development of a Comprehensive Analysis for Rotorcraft: Part I – Rotor Model and Wake Analysis," *Vertica*, **2**(5), pp. 99–129.

[76] Johnson, W. (1981) "Development of a Comprehensive Analysis for Rotorcraft: Part II – Aircraft Model, Solution Procedure, and Applications," *Vertica*, **5**(3), pp. 185–216.

[77] Johnson, W. (1980) *A Comprehensive Analytical Model of Rotorcraft Aerodynamics and Dynamics. Part 1. Analysis Development*, *Tech. rep.*, DTIC Document.

[78] Johnson, W. (1980) *A Comprehensive Analytical Model of Rotorcraft Aerodynamics and Dynamics. Part 2. User's Manual*, *Tech. rep.*, DTIC Document.

[79] Johnson, W. (1994) "Technology Drivers in the Development of CAMRAD II," in *American Helicopter Society Aeromechanics Specialists Conference, San Francisco, California*.

[80] Stephens, W. B., M. J. Rutkowski, R. A. Ormiston, and C. M. Tan (1989) "Development of the Second Generation Comprehensive Helicopter Analysis System(2 GCHAS)," in *AHS National Specialists' Meeting on Rotorcraft Dynamics, Arlington, TX, Proceedings*, vol. 13.

[81] Saberi, H., M. Khoshlahjeh, R. A. Ormiston, and M. J. Rutkowski (2004) "Overview of RCAS and Application to Advanced Rotorcraft Problems," in *American Helicopter Society 4th Decennial SpecialistsâĂŹ Conference on Aeromechanics, San Francisco, CA*.

[82] Bauchau, O. (2001) "DYMORE: A Finite Element Based Tool for the Analysis of Nonlinear Flexible Multibody Systems," *Georgia Inst. of Technology, Atlanta*.

[83] Johnson, W. (2013) "A History of Rotorcraft Comprehensive Analyses," in *Proceedings of the 69th American Helicopter Society Annual Forum*.

[84] Kufeld, R. M. and W. G. Bousman (1998) "High Load Conditions Measured on a UH-60A in Maneuvering Flight," *Journal of the American Helicopter Society*, **43**(3), pp. 202–211.

[85] Scarborough, L. H., III, C. D. Rahn, E. C. Smith, K. L. Koudela, and M. R. Jolly (2014) "Impedance Tailored Fluidic Pitch Links for Passive Hub Vibration Control and Improved Rotor Efficiency," in *Proceedings of the Fifth Decennial AHS Aeromechanics Specialists' Conference*.

[86] Zhang, J., L. H. Scarborough, III, E. C. Smith, C. D. Rahn, and M. R. Jolly (2014) "Evaluation of Fluidic Pitch Links for Rotor Hub Vibration Controls," in *Proceedings of the 40th European Rotorcraft Forum*.

[87] Milgram, J., I. Chopra, and S. Kottapalli (1994) "Dynamically Tuned Blade Pitch Links for Vibration Reduction," in *Proceedings of the 50th American Helicopter Society Annual Forum*.

[88] Han, D., C. D. Rahn, and E. C. Smith (2014) "Higher Harmonic Pitch Link Loads Reduction using Fluidlastic Isolators," in *Proceedings of the Institution of Mechanical Engineers, Part G: Journal of Aerospace Engineering*.

[89] Chopra, I. (1990) "Perspectives in Aeromechanical Stability of Helicopter Rotors," *Vertica*, **14**(4), pp. 457–508.

[90] Ham, N. D. (1973) *Helicopter Blade Flutter*, *AGARD 607*.

[91] Johnson, W. (2013) *Rotorcraft Aeromechanics*, chap. 16, Cambridge University Press, Cambridge, NY, pp. 666–670.

[92] Johnson, W. (2013) *Rotorcraft Aeromechanics*, chap. 20, Cambridge University Press, Cambridge, NY, pp. 788–795.

[93] Cafarelli, I., A. S. Hopkins, K. V. Truong, and T. Maier (2007) "Aeroelastic Stability Analysis of Two Hingeless Rotors," in *Proceedings of the 33rd European Rotorcraft Forum*.

[94] Johnson, W. (2013) *Rotorcraft Aeromechanics*, chap. 16, Cambridge University Press, Cambridge, NY, pp. 606–610.

[95] Johnson, W. (2013) *Rotorcraft Aeromechanics*, chap. 10, Cambridge University Press, Cambridge, NY, pp. 366–388.

[96] Peters, D. A. and K. H. Hohenemser (1971) "Application of the Floquet Transition Matrix to Problems of Lifting Rotor Stability," *Journal of the American Helicopter Society*, **16**(2), pp. 25–33.

[97] Friedmann, P. P., C. E. Hammond, and T.-H. Woo (1977) "Efficient Numerical Treatment of Periodic Systems with Application to Stability Problems," *International Journal for Numerical Methods in Engineering*, **11**(7), pp. 1117–1136.

[98] Jordan, D. W. and P. Smith (2007) *Nonlinear Ordinary Differential Equations: An Introduction for Scientists and Engineers*, 4 ed., Oxford University Press.

[99] Vahdati, N. (1998) "A Detailed Mechanical Model of a Double Pumper Fluid Mount," *Journal of Vibration and Acoustics*, **120**(2), pp. 361–370.

[100] Koivula, T. (2000) "On Cavitation in Fluid Power," in *Proceedings of the 1st FPNI Ph.D. Symposium on Fluid Power*, pp. 371–382.

[101] Treacy, S. M., C. D. Rahn, E. C. Smith, and C. Marr (2016) "Pitch-Flap Stability of an Articulated Rotor with Fluidic Pitch Links," in *Proceedings of the 2016 AHS Technical Meeting on Aeromechanics Design for Vertical Lift*.

[102] Romano, P. Q., M. Seifert, and M. Smith (2017) "The 505 Low Vibration Solution," in *Proceedings of the 73rd American Helicopter Society Annual Forum*.

[103] Horn, R. A. and C. R. Johnson (1990) *Matrix Analysis*, chap. 10, Cambridge University Press, New York, NY, pp. 313–386.

[104] Donovan, F., B. C. Taylor, and M. Su (1991) "One-Dimensional Computer Analysis of Oscillatory Flow in Rigid Tubes," *Journal of Biomechanical Engineering*, **113**(4), pp. 476–484.

[105] De Silva, C. W. (2005) *Vibration and Shock Handbook*, chap. 16, CRC Press, Boca Raton, FL, pp. 707–773.

[106] Brackbill, C. R., G. A. Lesieutre, E. C. Smith, and L. K. Byers (1996) "Formulation and Validation of a Thermomechanical Model for Elastomeric Materials," in *Proceedings of the 52nd American Helicopter Society Forum*, pp. 950–960.

[107] Brackbill, C. R., G. A. Lesieutre, E. C. Smith, and K. Govindswamy (1996) "Thermomechanical Modeling of Elastomeric Materials," *Smart Materials and Structures*, **5**(5), pp. 529–539.

[108] Marr, C., G. Lesieutre, and E. Smith (2008) "Nonlinear, Temperature-Dependent, Fluidlastic Lead-Lag Damper Modeling," in *Proceedings of the 64th American Helicopter Society Forum*, vol. 64.

[109] Marr, C., Z. Fuhrer, G. Lesieutre, and E. Smith (2011) "Multi-State Lead-Lag Damper Development and Validation," in *Proceedings of the 67th American Helicopter Society Forum*.

Vita

Shawn M. Treacy

Education

Doctor of Philosophy, Mechanical Engineering,
The Pennsylvania State University, December 2017.

Master of Science, Mechanical Engineering,
The Pennsylvania State University, May 2017.

Bachelor of Science, Mechanical Engineering,
Kettering University, December 2011.

Publications

Treacy, S. M., C. D. Rahn, E. C. Smith, and C. Marr, "Experimental Validation of a Fluidic Pitch Link Model," accepted by the 43^{rd} European Rotorcraft Forum, Milan, Italy, September 15–17, 2017.

Treacy, S. M., C. D. Rahn, E. C. Smith, and C. Marr, "Pitch-Flap Stability of an Articulated Rotor with Fluidic Pitch Links," *Proceedings of the 2016 AHS Technical Meeting Aeromechanics Design for Vertical Lift*, San Francisco, CA, January 20–22, 2016.